

SYNTHETIC OBSERVATIONS OF 21 CM H I LINE PROFILES FROM INHOMOGENEOUS TURBULENT INTERSTELLAR H I GAS WITH MAGNETIC FIELD

YASUO FUKUI,¹ TAKAHIRO HAYAKAWA,¹ TSUYOSHI INOUE,¹ KAZUFUMI TORII,² RYUJI OKAMOTO,¹ KENGO TACHIHARA,¹ TOSHIKAZU ONISHI,³ AND KATSUHIRO HAYASHI¹

¹Department of Physics, Nagoya University, Furo-cho, Chikusa-ku, Nagoya 464-8602, Japan

²Nobeyama Radio Observatory, National Astronomical Observatory of Japan, 462-2 Nobeyama, Minamimaki, Minamisaku, Nagano 384-1305, Japan

³Department of Physical Science, Osaka Prefecture University, 1-1 Gakuen, Sakai, Osaka 599-8531, Japan

(Received; Revised; Accepted)

Submitted to

ABSTRACT

We have carried out synthetic observations of interstellar atomic hydrogen at 21 cm wavelength by utilizing the theoretical results of magnetohydrodynamical numerical simulations of the inhomogeneous turbulent interstellar medium which includes both CNM and WNM (Inoue & Inutsuka 2012). We used the ultraviolet absorption measurements of H₂ in the local interstellar space in order to constrain the model parameters. We find the following: (1) The $W_{\text{H}\,\text{I}}\text{-}N_{\text{H}\,\text{I}}$ scatter plot shows a systematic change depending on T_s , (2) the contribution of H₂ in the $W_{\text{H}\,\text{I}}\text{-}N_{\text{H}\,\text{I}}$ plot is minor, indicating that “CO-free H₂” is not important, (3) the H I optical depth measured by absorption toward a radio continuum point source is significantly smaller than the optical depth derived from H I emission observed with large beams, because the covering factor of high H I optical-depth ($\tau_{\text{H}\,\text{I}} > 0.5$) regions is significantly small, $\sim 30\%$, as compared with that of low H I optical-depth regions, $\sim 70\%$. It is also found that the $W_{\text{H}\,\text{I}}\text{-}\tau_{353}$ (dust optical depth at 353 GHz) plot is better explained if dust evolution expressed as $N_{\text{H}\,\text{I}} + 2N_{\text{H}\,\text{2}} \propto \tau_{353}^{1/1.3}$ is taken into account. H I column density derived by emission-absorption (Heiles & Troland 2003a) is systematically smaller by a factor of ~ 1.7 than that corrected for the optically thick H I and for the dust evolution as is consistent with Fukui et al. (2014, 2015). The total mass of H I in the local interstellar space is accurately estimated to be 1.7-times the optically thin case by the latter method.

Keywords: ISM: atoms — ISM: clouds — radio lines: ISM

1. INTRODUCTION

The main constituent of the interstellar medium is atomic hydrogen H I, and the secondary constituents, whose abundance is ten times less than H I, include molecular hydrogen H₂ and atomic helium He over the global volume of the Galactic disk. It is of primary importance to make precise measurement of H I in our understanding of the structure, kinematics and physical conditions of the interstellar medium and the formation of interstellar clouds and stars.

The 21 cm spin flip transition of H I offers a direct method to measure interstellar H I and has been used extensively over the last several decades since its discovery in 1951 (Ewen & Purcell 1951; Muller & Oort 1951). When the H I 21 cm line is optically thin, the following equation is used to calculate the H I column density, $N_{\text{H I}}$, from the 21 cm line intensity, $W_{\text{H I}}$,

$$N_{\text{H I}} (\text{cm}^{-2}) = 1.823 \times 10^{18} W_{\text{H I}} (\text{K km s}^{-1}). \quad (1)$$

As such, it has been commonly thought that 21 cm H I emission is optically thin. Direct support for the optically thin assumption for H I by emission-absorption measurements toward radio continuum point sources, which shows that the H I peak optical depth is typically ~ 0.1 (e.g., Dickey et al. 2003; Heiles & Troland 2003a,b). High resolution H I observations with the Arecibo 305 m telescope have been used to make high sensitivity emission-absorption measurements and revolutionized the knowledge on the H I gas physical conditions (Heiles & Troland 2003b). In the meantime the question was raised that the 21 cm H I emission may be optically thick based on H I profiles with self-absorption (Braun 2012). Because H I observations provide physical quantities averaged along a line of sight, it is in principle impossible to retrieve the original physical parameters of the H I gas in the three dimensions, making it

difficult to test observationally the above H I properties for the large volume where H I is distributed.

The dust emission and extinction are also used often as a proxy for $N_{\text{H I}}$ under an assumption of constant gas to dust ratio. Previously, the scattering in the data for dust column density was large, making the method crude at best (see e.g., Chapter 21 of Draine 2011). Planck Collaboration (2014) opened a new possibility of precise measurement of dust optical depth by making extremely sensitive measurements of dust optical depth at sub-mm wavelengths, 350, 550 and 850 microns. These long wavelengths are in the Rayleigh-Jeans regime of the Planck function and, by combining the *IRAS* data at 100 microns in the Wien regime, the sub-mm dust optical depth and dust temperature for an appropriate dust emissivity β were calculated with unprecedented accuracy to within $\lesssim 10\%$.

Fukui et al. (2014, 2015) presented a method to use the *Planck* dust optical depth at 353 GHz (τ_{353}) as proxy of $N_{\text{H I}}$ by identifying the optically thin regime of 21 cm H I emission as a linear part of a scatter plot between $W_{\text{H I}}$ and τ_{353} , where dispersion of the data points is smallest at the highest dust temperature. Fukui et al. (2014) presented results for high-latitude clouds with the Galactic Arecibo L-band Feed Array H I (GALFA-H I) survey data (Peek et al. 2011) taken with a 4' beam of the Arecibo telescope and Fukui et al. (2015) for the whole sky at $|b|$ larger than 15° with a 33' beam in the Leiden/Argentine/Bonn (LAB) survey (Kalberla et al. 2005). The two papers concluded that, in the local interstellar volume within 200 pc of the sun, interstellar H I is dominated by cold and dense H I gas which is optically thick with a typical H I optical depth of ~ 1 , and that the average H I density is to be doubled approximately if the correction for the optical depth is applied. Fukui et al. (2015) ar-

gued that the opacity-corrected H I can explain the “dark gas”, which is detected in γ -rays and interstellar extinction A_V but not in the 2.6-mm CO or optically-thin 21-cm H I transitions (Grenier et al. 2005; Grenier et al. 2015 for a review), as an alternative to CO-free H₂ gas (Wolfire et al. 2010). In order to understand the behavior of H I, it is crucial to measure the fraction of H₂ in H I gas. Since H₂ has no radio transition, ultraviolet absorption of the electronic transition provides a unique tool to directly measure H₂. *FUSE* and *Copernicus* results are such datasets of H₂ (e.g., Gillmon et al. 2006). Since observations need background UV source, the H₂ observations measure H₂ in the local interstellar medium close to the sun. We are able to use the H₂ data in modeling the local interstellar medium. In some cases H I can be measured as well in UV. Also, H I measurements at 21 cm in line absorption toward radio continuum sources provide H I column density (e.g., Heiles & Troland 2003a,b).

There remain two issues which were not addressed in Fukui et al. (2014, 2015). One is the contribution of the warm neutral medium (WNM). Because the dust grains are included in the both phases, the cold neutral medium (CNM) and WNM, the H I emission analyzed with the *Planck* data should include the contribution of WNM. The other is the possible effect of dust evolution found by Roy et al. (2013) which may require some modification of the linear relationship between $N_{\text{H}\,\text{I}}$ and τ_{353} assumed by Fukui et al. (2014, 2015). Pioneering studies by Field (1965) and Field et al. (1969) showed that the interstellar medium consists of the two phases, CNM and WNM, which are in pressure equilibrium. H I emission-absorption measurements were used to constrain H I parameters of CNM and WNM (Dickey et al. 2003; Heiles & Troland 2003a,b), where WNM manifests itself as broad line wings of H I emission profiles. There remains yet an uncertainty in

deriving the WNM temperature in absorption, and only a lower limit for T_s was obtained to be around 300–1000 K, leaving the mass of WNM uncertain, which may occupy $\sim 60\%$ of total H I (Heiles & Troland 2003b).

Following Fukui et al. (2014, 2015), Stanimirović et al. (2014) made H I emission-absorption measurements toward radio continuum sources in Perseus with the Arecibo H I data and found that the absorption optical depth is not so large as suggested by Fukui et al. (2014, 2015), raising a question on the optically thick H I emission. Their results are consistent with those by Heiles & Troland (2003a,b). McKee et al. (2015) made a comparison of Fukui et al. (2015) with the H I model by Heiles et al. (1981) and discussed that the two results are consistent within $\sim 10\%$ in spite of their different H I optical depth. The reason for this agreement is not clarified. The method by Fukui et al. (2015) is based on a simple assumption of uniform interstellar medium and may need modification if realistic non-uniform physical properties of the interstellar medium are taken into account. The real H I observations are, however, limited because we are not able to assess the actual three dimensional physical conditions of the H I gas emitting/absorbing 21 cm line radiation.

A possible solution to overcome the difficulty and to test the above discrepancy is to utilize the results of hydrodynamical numerical simulations of the H I gas (Murray et al. 2015, 2016). Recently, three-dimensional hydrodynamical simulations modeled converging H I flows and achieved realistic density distributions and kinematics with high inhomogeneity and strong turbulence (Hennebelle et al. 2008; Heitsch et al. 2009; Banerjee et al. 2009; Vázquez-Semadeni et al. 2011; Inoue & Inutsuka 2012; Kim et al. 2014). These simulations are supported by observations of nearby galaxies which show turbulent H I gas with density of $10\text{--}100\,\text{cm}^{-3}$ and molecular clouds

formed from H I gas (Blitz & Rosolowsky 2006; Fukui et al. 1999, 2008, 2009; Kawamura et al. 2009; Fukui & Kawamura 2010).

In order to test the method by Fukui et al. (2015) and clarify the cause of the difference between the emission-absorption and emission measurements of H I, in the present paper we examine synthetic H I line profiles by using the data of magnetohydrodynamical (MHD) numerical simulations where the density, temperature, and velocity of the H I gas are available in three dimensions (Inoue & Inutsuka 2012). These simulations deal with converging H I flows as a function of time over 10 Myrs. The gas is originally H I, while formation of H₂ molecules is incorporated by using the usual dust surface reaction. The results indicate two phases of H I, CNM and WNM, as well as time-dependent transient gas which behaves intermediate. In the following we call for convenience the gas with T_s below 300 K CNM and that with T_s above 300 K WNM.

The present paper is organized as follows; Section 2 gives the results of the simulations, Section 3 presents results of synthetic observations with discussion and Section 4 describes the spatial distribution of the H I optical depth with discussion. In Section 5 we present the conclusions.

2. RESULTS OF SIMULATIONS

2.1. *Simulation Data and Model Selection*

We summarize the relevant physical parameters and symbols in Table 1. We then give a brief explanation of the physical parameters and settings of the MHD simulations. More details are found in Inoue & Inutsuka (2012). The simulations assume converging H I gas flows at 20 km s⁻¹ which are initially in pressure equilibrium with the standard interstellar H I having pressure of $pk_B^{-1} = 5.2 \times 10^3$ K cm⁻³. The x -, y - and z -axes are taken as in Figure 2 of Inoue & Inutsuka (2012) and the flow direction

is parallel to the x -axis. The H I gas flow is inhomogeneous and continuously enters into the box from the two opposite boundaries of a cube of (20 pc)³. In the interface of the converging flows turbulence is excited and the magnetic field is amplified. Formation of molecules such as H₂ formation on dust surfaces and CO formation via CH₂⁺ with the effects of self/dust UV shielding are taken into account and radiative and collisional heating and atomic and molecular cooling are incorporated. The simulation data are provided as the three dimensional data cube with 512³ uniform pixels¹ and each pixel having a size of 0.04 pc in each axis with the physical parameters as listed in Table 2. The simulations are made over a timescale of 10 Myrs, ten times the typical crossing timescale of the local H I gas in the solar neighborhood. The total gas mass in the numerical domain increases with time. Figure 1 compares the distribution of H I column density N_{H_1} and the fraction of H₂, $f_{\text{H}_2} = 2N_{\text{H}_2}/(2N_{\text{H}_2} + N_{\text{H}_1})$, where the integration was made for 10 pc along the y -axis. Data at the four time steps, 0.3, 0.5, 1 and 3 Myrs, are shown (see the physical parameters in Table 3). UV observations of f_{H_2} toward extragalactic sources (Gillmon et al. 2006) are shown by open circles in each panel and are summarized in Table 4, where the number of observed sources for f_{H_2} is limited to 19. We did not include Galactic OB stars which may be contaminated by localized gas (Rachford et al. 2002), possibly causing unreliable f_{H_2} values for the local ISM. The ranges of N_{H_1} and f_{H_2} are consistent with those of the synthetic data points, whereas the UV measurements are limited to $N_{\text{H}_2} \lesssim 10^{21}$ cm⁻². The trend that f_{H_2} increases with N_{H_1} is consistent with the synthetic data. Among the four time steps, we find the 0.5-Myr

¹ Inoue & Inutsuka (2012) made the simulations with dividing the numerical domain into 1024³ pixels but the data were provided at a factor-of-two lower resolution to reduce the data size.

Table 1. Summary of Symbols in the Text

Description	
T_k	Kinetic temperature of gas
$\tau_{\text{H I}}, T_s$	H I optical depth and spin temperature
$\tau_{\text{H I}}^{\text{abs}}, T_s^{\text{abs}}$	H I optical depth and spin temperature obtained by emission-absorption measurements (Eqs. 10 and 11)
$\tau_{\text{H I}}^F, T_s^F$	H I optical depth and spin temperature derived by applying the method presented by Fukui et al. (2015) (Eqs. 14 and 15)
$\langle T_s \rangle$	Density-weighted harmonic mean of T_s along a line-of-sight (Eq. 16)
T_b	Brightness temperature of H I spectrum
$W_{\text{H I}}$	Velocity integrated-intensity of H I spectrum
$W_{\text{H I}}^{\text{CNM}}$	$W_{\text{H I}}$ produced from CNM with $T_k < 300$ K
$W_{\text{H I}}^{\text{WNM}}$	$W_{\text{H I}}$ produced from WNM with $T_k > 300$ K
$N_{\text{H I}}$	H I column density
$N_{\text{H I}}^{\text{thin}}$	H I column density obtained under assumption of optically-thin H I line (Eq. 1)
$N_{\text{H I}}^{\text{HT}}$	Heiles & Troland (2003a) H I column density
$N_{\text{H I}}^F$	H I column density obtained from τ_{353} applying Equation (18) with assuming $N_{\text{H}_2} = 0$
$M_{\text{H I}}$	Mass of H I
$M_{\text{H I}}^{\text{thin}}$	Mass of H I obtained from $N_{\text{H I}}^{\text{thin}}$

Table 2. Summary of the Physical Parameters in the MHD model

Description	
n_X	Number densities of atomic/molecular species, $X = \text{H I}, \text{H}_2$ etc.
pk_{B}^{-1}	Thermal pressure of gas, $T_k = pk_{\text{B}}^{-1} (\sum_X n_X)^{-1}$
(V_x, V_y, V_z)	Velocity vector

model shows the best presentation of the observations since the fraction of the data points included within a 95% contour is the largest (14 out of 19). We shall use the 0.5-Myr model for the present analysis, whereas we do not exclude the 1.0-Myr model whose physical parameters are not significantly different from the 0.5-Myr

model. Figure 2 gives histograms of total column density $N_{\text{H I}} + 2N_{\text{H}_2}$ in the model and that of the observations by Fukui et al. (2015)². Figure 3 shows histograms of $n_{\text{H I}} + 2n_{\text{H}_2}$ and T_k in

² Fukui et al. (2015) obtained H I column densities assuming a linear relationship $N_{\text{H I}} \propto \tau_{353}$ but we ob-

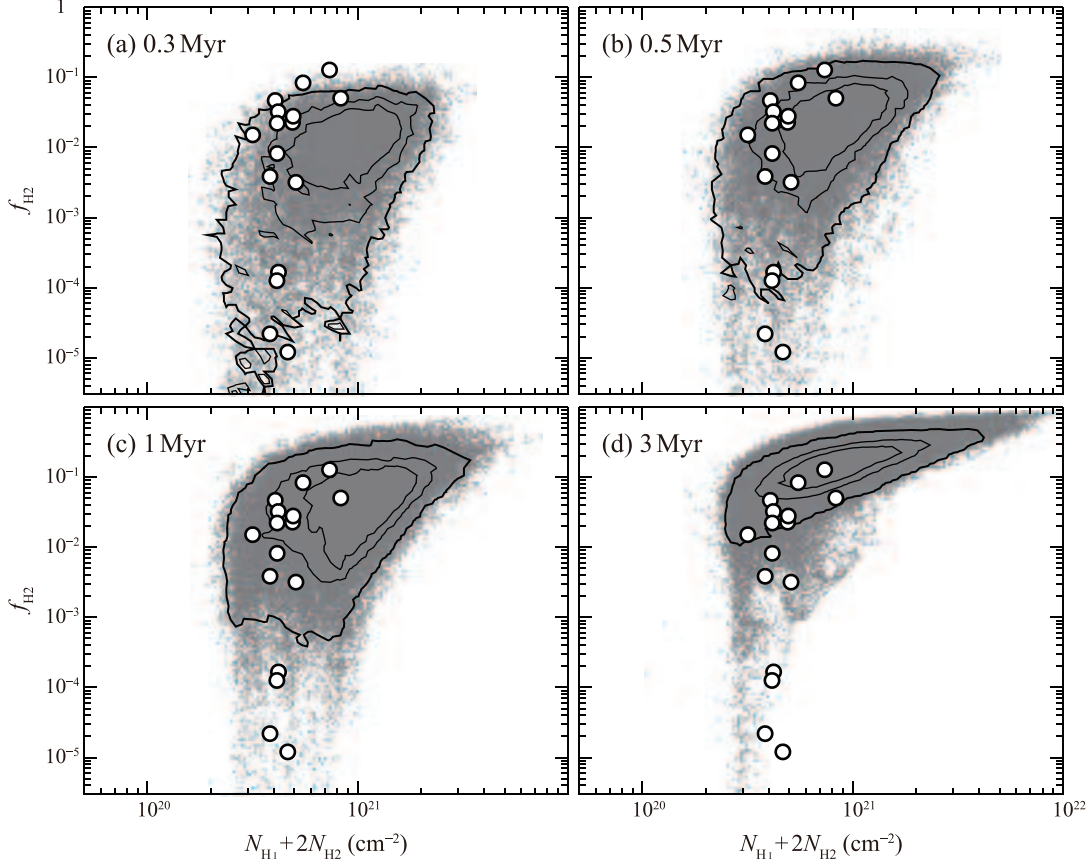


Figure 1. (a) Plot of molecular fraction defined as $f_{\text{H}2} = 2N_{\text{H}2}/(2N_{\text{H}1} + N_{\text{H}2})$ for total column density $N_{\text{H}1} + 2N_{\text{H}2}$ at a time step of 0.3 Myr. The contours includes 45%, 70% and 95% of data points. The open circles show the results of direct UV absorption measurements of H_2 by *FUSE* toward AGNi (summarized in Table 4, 3 out of 19 are not shown due to low $f_{\text{H}2} \sim 10^{-6}$). (b)–(d) Same as (a) but at time steps of 0.5 Myr, 1 Myr, and 3 Myr, respectively.

the model. We find that these physical parameters have large ranges covering CNM and WNM, whereas the two phases are not so clear due to intermediate gas formed by the strong turbulent mixing in the model. The molecular gas is peaked at the densest and coldest regime. Note that the typical ISM is affected by supernovae with every a few million years and duration of compression (or lifetime of a supernova shock) is about 1 million years. The ISM compressed by the converging flows in the 0.5–1.0 Myr seems to be the representative state of the dynamic ISM.

tained total column densities by applying a nonlinear relationship $N_{\text{H}1} + 2N_{\text{H}2} \propto \tau_{353}^{1/1.3}$ (see Section 3.5).

2.2. Calculations of H I Line Profiles

The basic equations in the synthetic observations are line radiation transfer as given by equations

$$I_{j+1}(V) = I_j(V) \exp[-\kappa_j(V)\Delta y] + \frac{\epsilon_j(V)}{\kappa_j(V)} \{1 - \exp[-\kappa_j(V)\Delta y]\}$$

$$I_0 = B(T_{\text{bg}}) \sim \frac{2\nu_0^2}{c^2} k_B T_{\text{bg}},$$

where $I(V)$ the line intensity, $\kappa(V)$ opacity, $\epsilon(V)$ emissivity, $B(T)$ the Planck function at 21 cm, $\nu_0 = 1.420405751$ GHz, $T_{\text{bg}} = 2.7$ K the brightness temperature of the background radiation field, c the light velocity and k_B Boltzmann constant. The subscript j stands for the j -th cell along a line of sight. The emissivity ϵ

Table 3. Physical parameters from the models at different time steps

Time step (Myr)	$M_{\text{H I}}$ (M_{\odot})	$M_{\text{H I}}^{\text{thin}}$ (M_{\odot})	$\frac{M_{\text{H I}}}{M_{\text{H I}}^{\text{thin}}}$	M_{H2} (M_{\odot})	$\frac{M_{\text{H2}}}{M_{\text{H2}} + M_{\text{H I}}}$
(1)	(2)	(3)	(4)	(5)	(6)
0.3	581	508	1.1	4.7	8.1×10^{-3}
0.5	742	634	1.2	20.8	2.7×10^{-2}
	(394) ^a	(306) ^a	(1.3) ^a	(18.8) ^a	$(4.6 \times 10^{-2})^a$
1.0	1052	848	1.2	86.9	7.6×10^{-2}
3.0	1893	1257	1.5	690.8	2.7×10^{-1}

^aThe values in the masked region shown in Figure 6(a).

NOTE— Columns (2): mass of H I gas, (3): mass of H I given from H I integrated-intensity under optically-thin assumption, (4): ratio of (2) to (3), (5): mass of H₂ gas, (6): mass fraction of H₂ gas.

and opacity κ of the 21 cm transition at a radial velocity V are calculated as follows;

$$\epsilon_j(V) = \frac{hc}{4\pi} n_{\text{up},j} A \phi_j(V), \quad (4)$$

$$\kappa_j(V) = \frac{3c^3 h}{8\pi\nu_0^2 k_B T_{\text{s},j}} n_{\text{low},j} A \phi_j(V), \quad (5)$$

where h and $A = 2.8688754 \times 10^{-15} \text{ s}^{-1}$ are the Planck constant and the Einstein A coefficient, respectively. The number density of H atom in the lower state is given by

$$n_{\text{low},j} = \frac{n_{\text{H I},j}}{3 \exp\left(\frac{-h\nu_0}{k_B T_{\text{s},j}}\right) + 1} \quad (6)$$

and that in the upper state is

$$n_{\text{up},j} = n_{\text{H I},j} - n_{\text{low},j} \quad (7)$$

for total H I density $n_{\text{H I}}$. The line shape function

$$\phi_j(V) = \sqrt{\frac{m_{\text{p}} + m_{\text{e}}}{2k_B T_{\text{s},j}\pi}} \exp\left[\frac{-(m_{\text{p}} + m_{\text{e}})(V - V_{y,j})^2}{2k_B T_{\text{s},j}}\right] \quad (8)$$

satisfies $\int \phi(V)dV = 1$, where $m_{\text{p}} = 1.67262178 \times 10^{-24} \text{ g}$ is the mass of a proton and $m_{\text{e}} = 9.10938291 \times 10^{-28} \text{ g}$ is that of an electron. The H I spin temperature T_{s} is derived by applying a method by [Kim et al. \(2014\)](#), which gives $T_{\text{s}} \sim T_{\text{k}}$ in a T_{k} range from 20 to $3 \times 10^3 \text{ K}$. For $T_{\text{k}} < 20 \text{ K}$, we simply adopt $T_{\text{s}} = T_{\text{k}}$. The $\sim 75\%$ of the data pixels have $T_{\text{s}}/T_{\text{k}} = 0.9\text{--}1.0$ and the others $T_{\text{s}}/T_{\text{k}} = 0.8\text{--}0.9$.

Figures 4(a)–(d) show H I profiles along a certain line of sight, density n , temperature T_{k} , line-of-sight velocity V_y and peak opacity κ^{peak} . An H I line profile is calculated by integrating the line transfer Equations (2) and (3) from the far side to the near side of the data cube along the y -axis seen by the observer over a distance of 10 pc, a half of the full span of the data cube, and the observed brightness temperature is given by

$$T_{\text{b}}(V) = I(V) \frac{c^2}{2\nu_0^2 k_{\text{B}}} - T_{\text{bg}}. \quad (9)$$

Table 4. Parameters of the f_{H_2} Estimates

Target	l	b	N_{H_2} (cm^{-2})	τ_{353}	$N_{\text{H}_1} + 2N_{\text{H}_2}$ (cm^{-2})	f_{H_2}
(1)	(2)	(3)	(4)	(5)	(6)	(7)
3C 249.1	130°39	+38°55	9.5×10^{18}	2.51×10^{-6}	4.1×10^{20}	4.7×10^{-2}
ESO 141-G55	338°18	-26°71	2.1×10^{19}	6.38×10^{-6}	8.3×10^{20}	5.0×10^{-2}
H1821+643	94°00	+27°42	8.1×10^{17}	3.37×10^{-6}	5.1×10^{20}	3.2×10^{-3}
HE 1143-1810	281°85	+41°71	3.5×10^{16}	2.63×10^{-6}	4.2×10^{20}	1.7×10^{-4}
MRC 2251-178	46°20	-61°33	3.5×10^{14}	1.23×10^{-6}	2.3×10^{20}	3.0×10^{-6}
Mrk 9	158°36	+28°75	2.3×10^{19}	3.73×10^{-6}	5.5×10^{20}	8.4×10^{-2}
Mrk 335	108°76	-41°42	6.8×10^{18}	2.62×10^{-6}	4.2×10^{20}	3.2×10^{-2}
Mrk 509	35°97	-29°86	7.4×10^{17}	2.33×10^{-6}	3.8×10^{20}	3.9×10^{-3}
Mrk 1383	349°22	+55°12	2.2×10^{14}	1.55×10^{-6}	2.8×10^{20}	1.6×10^{-6}
Mrk 1513	63°67	-29°07	2.6×10^{16}	2.57×10^{-6}	4.1×10^{20}	1.3×10^{-4}
MS 0700.7+6338	152°47	+25°63	5.6×10^{18}	3.21×10^{-6}	4.9×10^{20}	2.3×10^{-2}
NGC 7469	83°10	-45°47	4.7×10^{19}	5.44×10^{-6}	7.4×10^{20}	1.3×10^{-1}
PG 0804+761	138°28	+31°03	4.6×10^{18}	2.58×10^{-6}	4.1×10^{20}	2.2×10^{-2}
PG 0844+349	188°56	+37°97	1.7×10^{18}	2.58×10^{-6}	4.1×10^{20}	8.2×10^{-3}
PG 1211+143	267°55	+74°32	2.4×10^{18}	1.82×10^{-6}	3.2×10^{20}	1.5×10^{-2}
PG 1302-102	308°59	+52°16	4.2×10^{15}	2.33×10^{-6}	3.8×10^{20}	2.2×10^{-5}
PKS 0558-504	257°96	-28°57	2.8×10^{15}	3.00×10^{-6}	4.7×10^{20}	1.2×10^{-5}
PKS 2155-304	17°73	-52°25	1.5×10^{14}	7.92×10^{-7}	1.7×10^{20}	1.8×10^{-6}
VII Zw 118	151°36	+25°99	6.9×10^{18}	3.24×10^{-6}	4.9×10^{20}	2.8×10^{-2}

NOTE— Columns (1): name of target, (2) and (3): position in the Galactic coordinates, (4): H_2 column density derived with the UV measurements (Gillmon et al. 2006), (5): dust optical depth at 353 GHz (Planck Collaboration 2014), (6): total column density obtained from τ_{353} taking into account a nonlinear relationship (see Section 3.5), (7): H_2 fraction given by $f_{\text{H}_2} = 2N_{\text{H}_2}/(2N_{\text{H}_2} + N_{\text{H}_1})$.

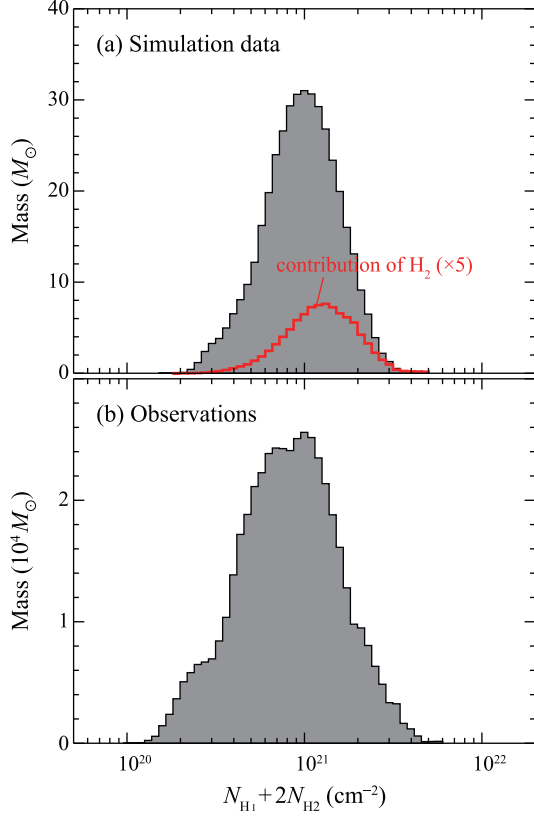


Figure 2. (a) Mass histograms of total column density, $N_{\text{H}\text{I}} + 2N_{\text{H}_2}$ in the 0.5-Myr model. The red line represents the contribution of H_2 (multiplied by a factor of 5). (b) Same as (a) but for the observational dataset used in Fukui et al. (2015). Here the total column densities are given from τ_{353} (Planck Collaboration 2014) by taking into account a nonlinear relationship (see Section 3.5).

The calculated H I profiles are given in Figure 5(a) for three different directions. Figure 5(a) shows three emission line profiles; the black solid line is the emission of the whole H I gas, and the gray-solid and dashed lines give the emission from the warm gas with T_s higher than 300 K and 1000 K, respectively. The profiles only from the hot gas are calculated by setting the emissivity ϵ of the cold gas equal to 0, while the opacity κ of the whole gas is held fixed. Figure 5(b) shows a subtraction of the hot gas profile higher than 300 K from the whole emission profile.

Figure 5(c) shows the absorption spectra obtained from the emission-absorption measurement given as,

$$1 - \exp[-\tau_{\text{H}\text{I}}^{\text{abs}}(V)] = \frac{T_{\text{b},\text{off}}(V) - T_{\text{b},\text{on}}(V)}{T_{\text{cont}} - 2.7 \text{ K}}, \quad (10)$$

Figure 5(d) $\tau_{\text{H}\text{I}}^{\text{abs}}$, and Figure 5(e) the spin temperature profile given as,

$$T_s^{\text{abs}}(V) = \frac{T_{\text{b},\text{off}}(V)}{1 - \exp[-\tau_{\text{H}\text{I}}^{\text{abs}}(V)]} + 2.7 \text{ K}, \quad (11)$$

which are given by the off-source brightness temperature $T_{\text{b},\text{off}}$ and on-source brightness temperature $T_{\text{b},\text{on}}$;

$$T_{\text{b},\text{off}}(V) = [T_s(V) - 2.7 \text{ K}] \{1 - \exp[-\tau_{\text{H}\text{I}}(V)]\}, \quad (12)$$

and

$$T_{\text{b},\text{on}}(V) = [T_s(V) - T_{\text{cont}}] \{1 - \exp[-\tau_{\text{H}\text{I}}(V)]\}. \quad (13)$$

Here T_{cont} is the temperature of an assumed background compact continuum source. The actual observational sensitivity is, however, limited by the observational noise levels and there is an observational lower limit of T_s^{abs} which is usually estimated to be 300–1000 K (Dickey et al. 2003; Heiles & Troland 2003a,b).

3. RESULTS OF THE SYNTHETIC OBSERVATIONS

3.1. H I emission profiles

In Figure 5(a) the H I emission profile consists of two parts, the narrow component and the broad wing-like component. The narrow component is in a velocity range from -5 km s^{-1} to $+5 \text{ km s}^{-1}$ and the wing component is extended in a range from -20 km s^{-1} to $+20 \text{ km s}^{-1}$. The total intensity integrated over velocity gives the total intensity of the 21 cm line emission $W_{\text{H}\text{I}}$. Contribution of WNM is indicated for $T_s > 300$ –1000 K, where self absorption by CNM is taken into account.

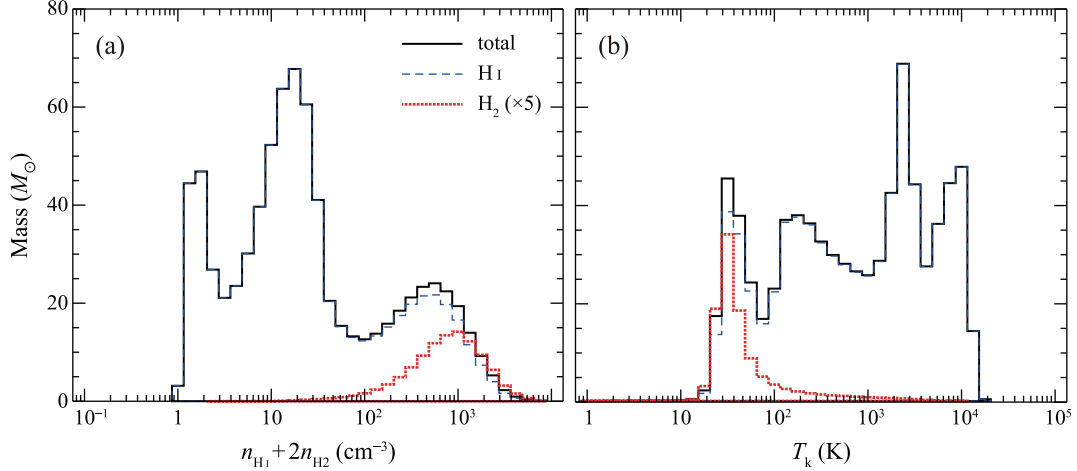


Figure 3. Mass histograms of (a) total hydrogen density ($n_{\text{H}_1} + 2n_{\text{H}_2}$) and (b) kinetic temperature (T_k) for each pixel in the 0.5-Myr model. The blue-long-dashed lines represents the contribution of H I and the red-short-dashed lines represent that of H₂ (multiplied by a factor of 5).

3.2. H I absorption profiles

Absorption line profiles are determined mainly by CNM whose H I optical depth is generally large (Figure 5(c)) and they consist of the narrow component. It is notable that the observed solid angle where absorption has been observed corresponds to a few tens of square arc seconds which is much smaller than the beam size of the H I emission measurement 4' (the Arecibo beam), and 33' (the LAB-survey beam). The spatial power spectrum of the H I emission fluctuations (Crovisier & Dickey 1983) affects the variation over one or two beam widths in the emission $T_{\text{b,off}}$ (Equation (12)), which limits practically the precision of H I optical depth in absorption in Equation (10). N_{H_1} of the broad component in emission is calculated by the optically thin approximation, though the narrow component is a mixture of both CNM and WNM. It is impossible to discern CNM and WNM from a single observed intensity at V . This causes an uncertainty in the mass of the WNM, and only lower limits of T_s are given at 300–1000 K (Dickey et al. 2003; Heiles & Troland 2003b). The WNM mass is guessed to be ∼60% of that of N_{H_1} , but it is uncertain (Dickey et al. 2003; Heiles & Troland 2003b). The present synthetic observations

show that the fraction of WNM in W_{H_1} of the narrow component varies from 30% to 70% (cf., Figure 5(a) and Table 5).

3.3. Application of the method by Fukui et al. (2015)

Once W_{H_1} and N_{H_1} are given, we are able to apply the method presented by Fukui et al. (2015) to the synthetic observations. In the method, a uniform single layer of H I gas is assumed and the sub-mm dust optical depth is used as proxy for the total gas column density on the assumption that the sub-mm dust radiation properties are uniform per proton. The method allows one to solve the two equations

$$W_{\text{H}_1} = (T_s^{\text{F}} - T_{\text{bg}}) \Delta V_{\text{H}_1} [1 - \exp(-\tau_{\text{H}_1}^{\text{F}})] \quad (14)$$

and

$$\tau_{\text{H}_1}^{\text{F}} = \frac{N_{\text{H}_1}(\text{cm}^{-2})}{1.823 \times 10^{18}} \frac{1}{T_s^{\text{F}}(\text{K}) \Delta V_{\text{H}_1}(\text{km s}^{-1})} \quad (15)$$

to obtain T_s^{F} and $\tau_{\text{H}_1}^{\text{F}}$ averaged over the linewidth ΔV_{H_1} . Here N_{H_1} and the linewidth ΔV_{H_1} are calculated by $N_{\text{H}_1} = \sum_j (n_{\text{H}_1,j} \Delta y)$, which is an exact value in the model, and $\Delta V_{\text{H}_1} = W_{\text{H}_1} / \max[T_{\text{b}}(V)]$, respectively. Figures 6(a)–(d) show two-dimensional distributions of N_{H_1} , W_{H_1} , T_s^{F} , and $\tau_{\text{H}_1}^{\text{F}}$ in the sky.

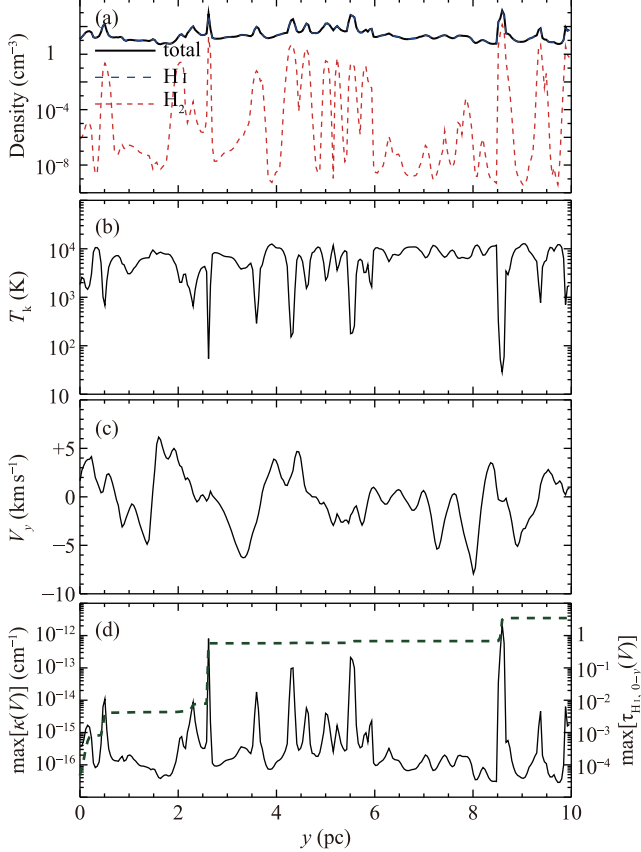


Figure 4. (a) Density profile along a line of sight; red-short-dashed, blue-long-dashed and black-solid lines show $n_{\text{H}2}$, $n_{\text{H}1}$, and $n_{\text{H}1} + 2n_{\text{H}2}$, respectively. The horizontal axis is the distance from the far-side of the model ISM, y . Profiles of (b) T_k , (c) line-of-sight velocity, V_y , and (d) peak opacity, $\max[\kappa(V)]$ given by Equation (5), along the same line of sight as (a) are also shown. Peak optical depth $\max[\tau_{\text{H}1,0-y}(V)] = \max[\int_0^y \kappa(V) dy']$ is plotted against right-side vertical-axis of panel (d) by the dashed line.

It was discussed that T_s affects the emission profile via a density-weighted harmonic mean in a line of sight (Dickey et al. 2003) calculated as follows,

$$\frac{\sum_j (n_{\text{H}1,j})}{\langle T_s \rangle} = \sum_j \left(\frac{n_{\text{H}1,j}}{T_{s,j}} \right) \quad (16)$$

Figure 7(a) shows a scatter plot between T_s^F and $\langle T_s \rangle$, showing a good correlation with a correlation coefficient of 0.93. This is consistent with that T_s derived by Fukui et al. (2014, 2015), T_s^F ,

is a density-weighted harmonic mean of T_s along a line of sight, and is mainly governed by CNM with low T_s .

The H I optical depth at a radial velocity V , $\tau_{\text{H}1}(V)$, obtained by integration in a line of sight is calculated as follows;

$$\tau_{\text{H}1}(V) = \sum_j [\kappa_j(V) \Delta y]. \quad (17)$$

Figure 7(b) shows a good correlation between velocity-integrated values of H I optical depth, $\int \tau_{\text{H}1}(V) dV$ and $\tau_{\text{H}1}^F \Delta V_{\text{H}1}$, with a correlation coefficient of 0.65. We thus confirm that spin temperature derived by the method T_s^F is well represented by the density-weighted harmonic mean of T_s and $\tau_{\text{H}1}^F$ corresponds to velocity averaged $\tau_{\text{H}1}$ along a line of sight. WNM was not apparent in the results of Fukui et al. (2014, 2015). This is understandable because T_s and $\tau_{\text{H}1}$ are almost exclusively dominated by CNM. The H I parameters obtained by the method therefore have clear physical meanings. In the method $N_{\text{H}1}$ is correctly calculated from τ_{353} with modification by Equation (18) as discussed in Section 3.5.

3.4. Scatter plot of $W_{\text{H}1}$ versus $N_{\text{H}1}$

Figure 8(a) shows scatter plots between $W_{\text{H}1}$ and $N_{\text{H}1}$, where T_s^F is indicated by different colors. The plot as a whole shows a large scatter, lending support for the ideal optically thick H I. The optical depth increases with decreasing T_s , where the highest T_s^F above 200 K is in the optically thin regime. For T_s^F below 60 K the H I optical depth becomes $\gtrsim 1.0$ and saturation in $W_{\text{H}1}$ is significant. $W_{\text{H}1}$ decreases by a factor of $\gtrsim 2$ –3 as compared with the optically thin case. The optically thin limit at highest T_s shows the smallest dispersion in $W_{\text{H}1}$ and $N_{\text{H}1}$, whereas the dispersions become larger with decrease of T_s . This is because the optical depth and the saturation degree in $W_{\text{H}1}$ become larger with decrease of T_s . The optically thin and thick

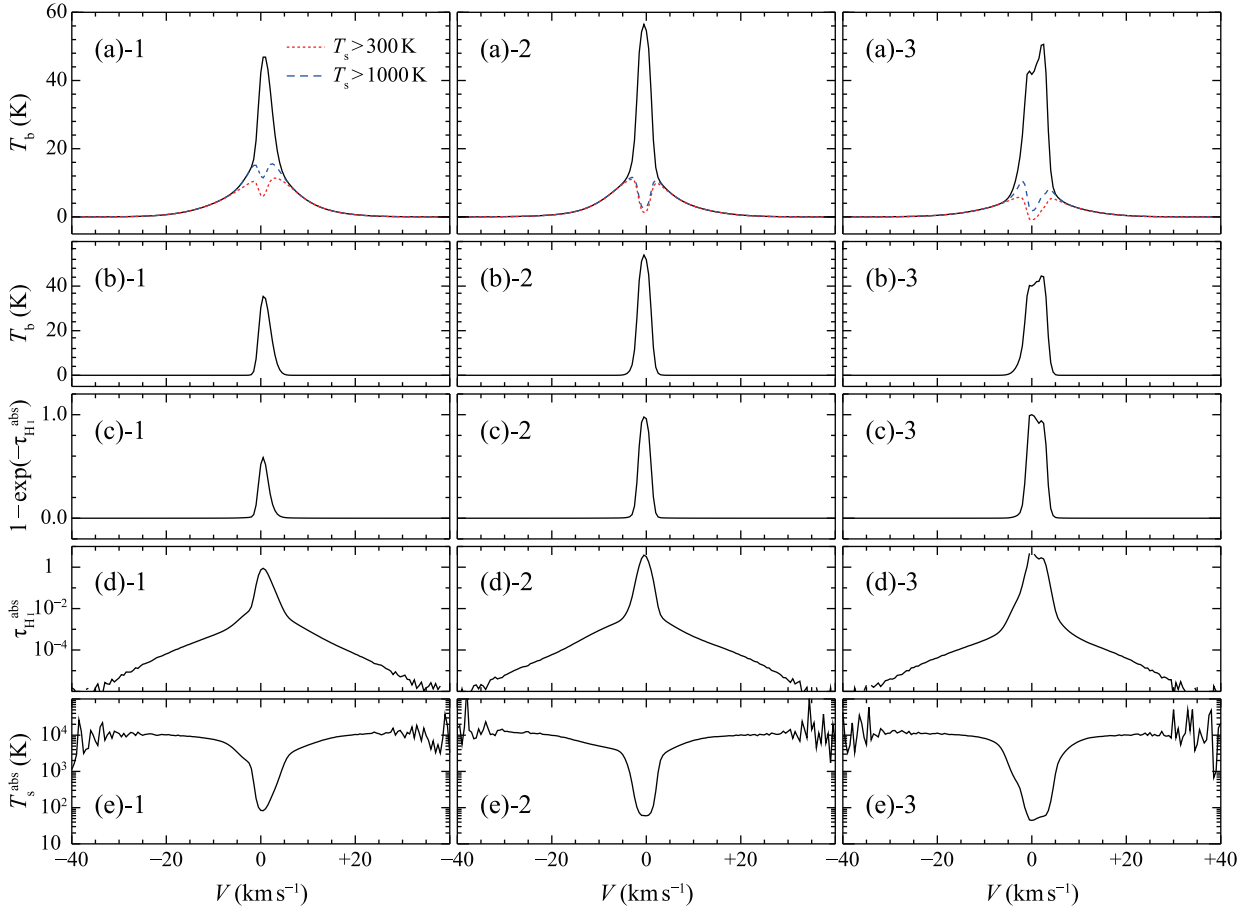


Figure 5. (a) Synthetic-observed H I emission spectra toward the different three directions. The black solid lines are the emission of the whole H I gas, and the short-dashed- and long-dashed-lines give the emission from the warm gas with T_s higher than 300 K and 1000 K, respectively. The profiles only from the hot gas are calculated by setting the emissivity ϵ of the cold gas equal to 0, while the opacity κ of the whole gas is held fixed. (b) Subtraction of the hot gas profiles (higher than 300 K) from the whole emission profiles. (c) and (d) Absorption spectra given by Equation (10). (e) The spin-temperature profile obtained by emission-absorption measurements (Equation (11)).

regimes are consistent with what were found by Fukui et al. (2014, 2015).

The H₂ fraction f_{H_2} was used to constrain the model in Section 2.1. In the present model the overall ratio f_{H_2} is $\sim 3\%$ (Table 3). Figure 8(b)-1 shows a case where both H I and H₂ are counted, whereas Figure 8(a)-1 a case with only H I. The inclusion of H₂ shows little difference, indicating that H₂ does not affect the W_{H_1} - N_{H_1} correlation significantly. Figure 8(c)-1 shows the difference for some of the data points is small, supporting this conclusion. Figures 8(a)-2, 8(b)-2, and 8(c)-2 show close up versions of the same figures. The diagrams indicate

CO-free H₂ does not account for the decrease of W_{H_1} with N_{H_1} , which is not explained by H I-H₂ conversion claimed in previous papers (e.g., Liszt 2014). The present conclusion holds in the local interstellar space within 200 pc of the sun where the crossing timescale 10^6 yrs is too short to form H₂ for H I density of 100 cm^{-3} (e.g., Inoue & Inutsuka 2012), and is not to be confused with a system having a longer timescale. For instance, H I envelopes of giant molecular clouds having timescales of $\gtrsim 10^7$ yrs may form CO-free H₂ (Wolfire et al. 2010).

In order to clarify the connection between the observed quantities and the physical parameters

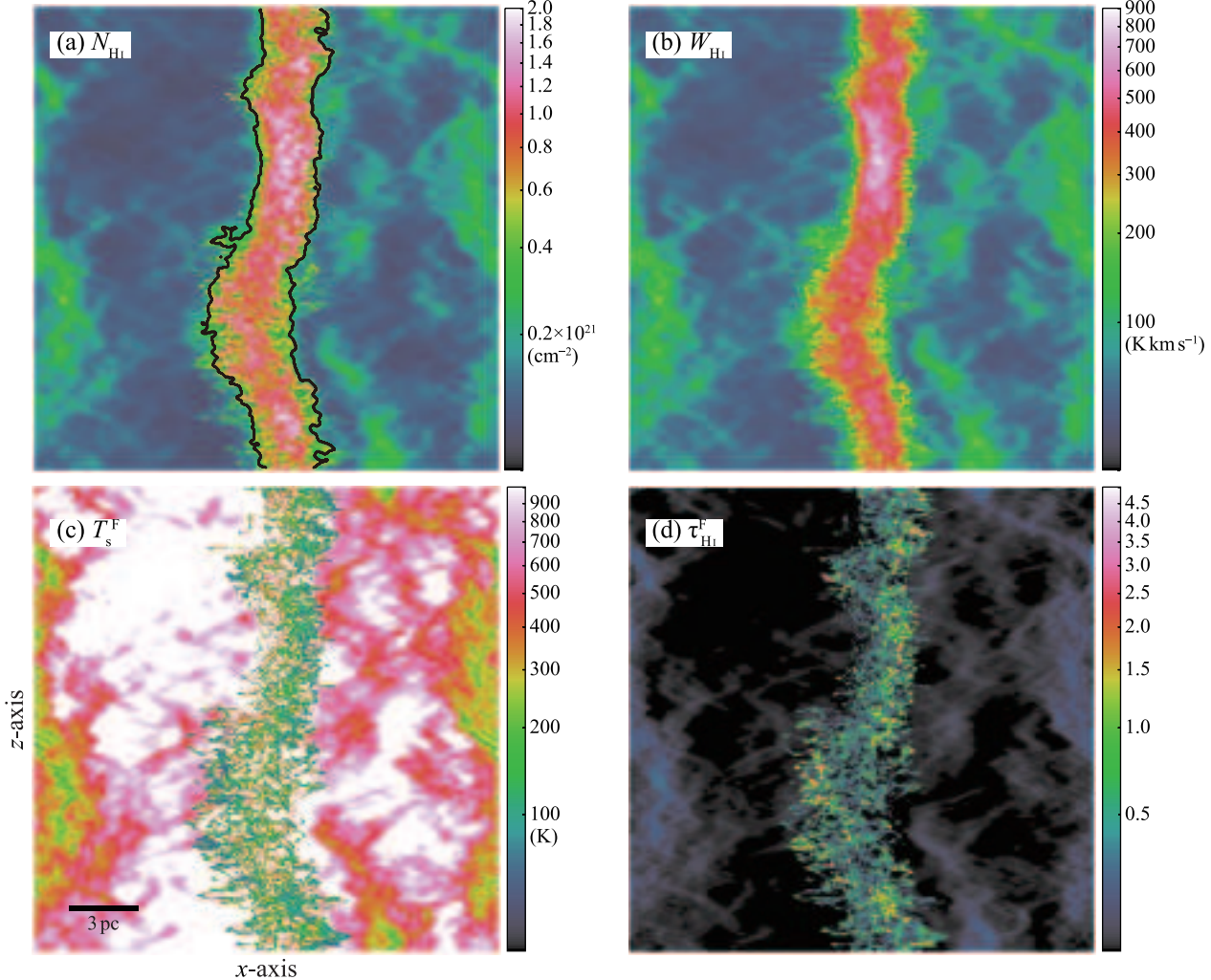


Figure 6. Spatial distribution of (a) theoretically-given H I column density (N_{HI}) and (b) velocity-integrated intensity of the synthetic-observed H I spectra (W_{HI}) in the 0.5-Myr model. Those of the H I spin temperature (T_s^F) and optical depth (τ_{HI}^F) derived by applying the method presented by Fukui et al. (2015) are shown in panels (c) and (d), respectively. The images are $20\text{ pc} \times 20\text{ pc}$ in size and have a resolution of 0.04 pc per pixel. The x axis in the numerical domain corresponds to the horizontal axis of each panel and the z axis to the vertical axis. The contour in panel (a) outlines the masked region applied in Figures 2(a), 7, 8 and 13.

in the model, we compare three H I profiles with different optical depth in Figure 5(a). They all have $W_{\text{HI}} = 350\text{ K km s}^{-1}$. We give breakdowns of τ_{HI} for CNM and WNM in Table 5. The smallest N_{HI} corresponds to $\langle T_s \rangle = 200\text{ K}$ and the H I emission is completely optically thin, i.e., both CNM and WNM are optically thin. The second with intermediate N_{HI} having $\langle T_s \rangle = 82\text{ K}$ is partially saturated and the third with the largest N_{HI} having $\langle T_s \rangle = 33\text{ K}$ is most heavily saturated by optical depth; looking in

more detail in these two profiles $W_{\text{HI}}^{\text{CNM}}$ is saturated and $W_{\text{HI}}^{\text{WNM}}$ stays optically thin. Table 5 lists the physical parameters, T_s^F and τ_{HI}^F , for CNM and WNM in the three profiles. Because in WNM T_s^F is higher than 300 K and the line intensity is less than 30 K , τ_{HI} of the WNM is less than 0.1 in the three profiles. Optically thin $W_{\text{HI}}^{\text{WNM}}$ is approximated by a product of high T_k (above $\sim 300\text{ K}$) and small τ_{HI} (below ~ 0.1). T_s^F is a mass-weighted harmonic mean and is always governed by T_s^F of the CNM. On the other

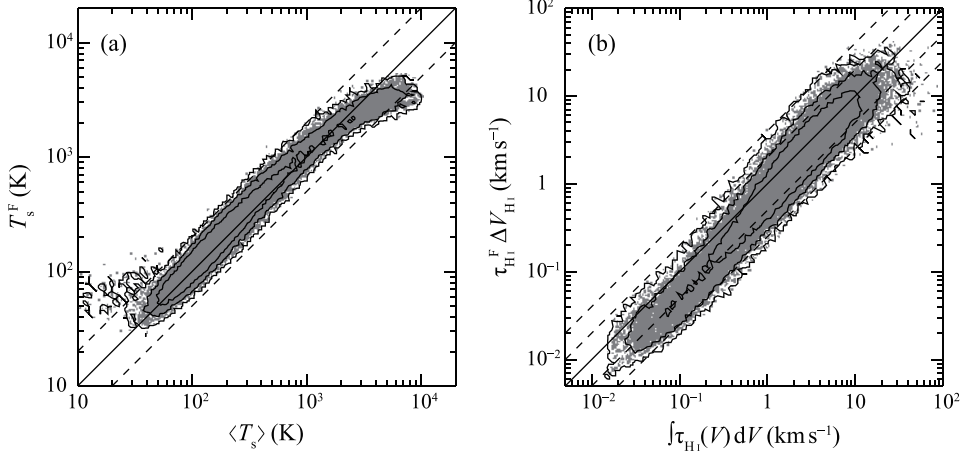


Figure 7. (a) Scatter plot between density-weighted harmonic mean spin temperature, $\langle T_s \rangle$ (see Section 3.3), and T_s^F . The straight solid lines indicate $T_s^F = \langle T_s \rangle$ and dashed lines indicate $T_s^F = \langle T_s \rangle/2$ or $T_s^F = 2\langle T_s \rangle$. Contours include 68%, 95% and 99.7% of data points. (b) Same as (a) but for velocity-integrated H I optical depth, $\int \tau_{\text{H I}}(V) dV$, and $\tau_{\text{H I}}^F \Delta V_{\text{H I}}$.

hand, $W_{\text{H I}}^{\text{CNM}}$ becomes saturated more with the decrease of T_s .

It was thought that the H I profiles often show self-absorption dips if the line is optically thick. In order to test if this is correct, we calculated the synthetic H I profiles both in emission and absorption and compared the peak velocity between them. We find that in many profiles ($\sim 90\%$) the peak velocities in emission and absorption agree well (within 0.5 km s^{-1}) in the present model. This means self-absorption dips are not a common signature of self-absorption. The reason is the appearance of self-absorption dips depends on the line-of-sight distribution of CNM, and high optical-depth cold clouds are not always in front of the brighter clouds.

3.5. Signature of dust evolution

Roy et al. (2013) suggested that dust evolution may take place in the Orion A cloud based on a comparison of H I gas with near infrared extinction A_J as expressed by $N_{\text{H}} \propto A_J^{1/1.28}$. Okamoto et al. (2016) find evidence which supports this conclusion in the Perseus and Chameleon regions based on $W_{\text{H I}} - \tau_{353}$ correlation and a comparison with A_J . Okamoto et al. (2016) presented a new nonlinear relationship between $N_{\text{H I}} + 2N_{\text{H}_2}$ and τ_{353} expressed as fol-

lows;

$$N_{\text{H I}} + 2N_{\text{H}_2} = \left(\frac{\tau_{353}}{1 \times 10^{-6}} \right)^{1/1.3} \times 2 \times 10^{20} \text{ (cm}^{-2}\text{)}. \quad (18)$$

Figure 9 shows the result where Equation (18) is applied to the data points in Fukui et al. (2015). Figure 9(a) shows the original plot assuming a linear relationship and Figure 9(b) the corrected plot by Equation (18). We find the nonlinear equation shows a radial distribution, passing through the origin, of data points with dust temperature $T_d \gtrsim 20 \text{ K}$ for given T_s and is better fitted to Figure 8, whereas the linear relationship shows a mildly curved shape which does not agree with Figure 8. We therefore infer the nonlinear relation gives reasonable conversion of τ_{353} into $N_{\text{H I}} + 2N_{\text{H}_2}$, and adopt Equation (18) in the following.

4. SPATIAL DISTRIBUTION OF H I OPTICAL DEPTH

The present MHD simulations demonstrate the details of spatial distribution of CNM and WNM. Figures 10 (a) and (b) show the distribution of $W_{\text{H I}}$ for CNM and WNM, respectively. It is important to note that the covering factor of CNM, which is generally optically thick,

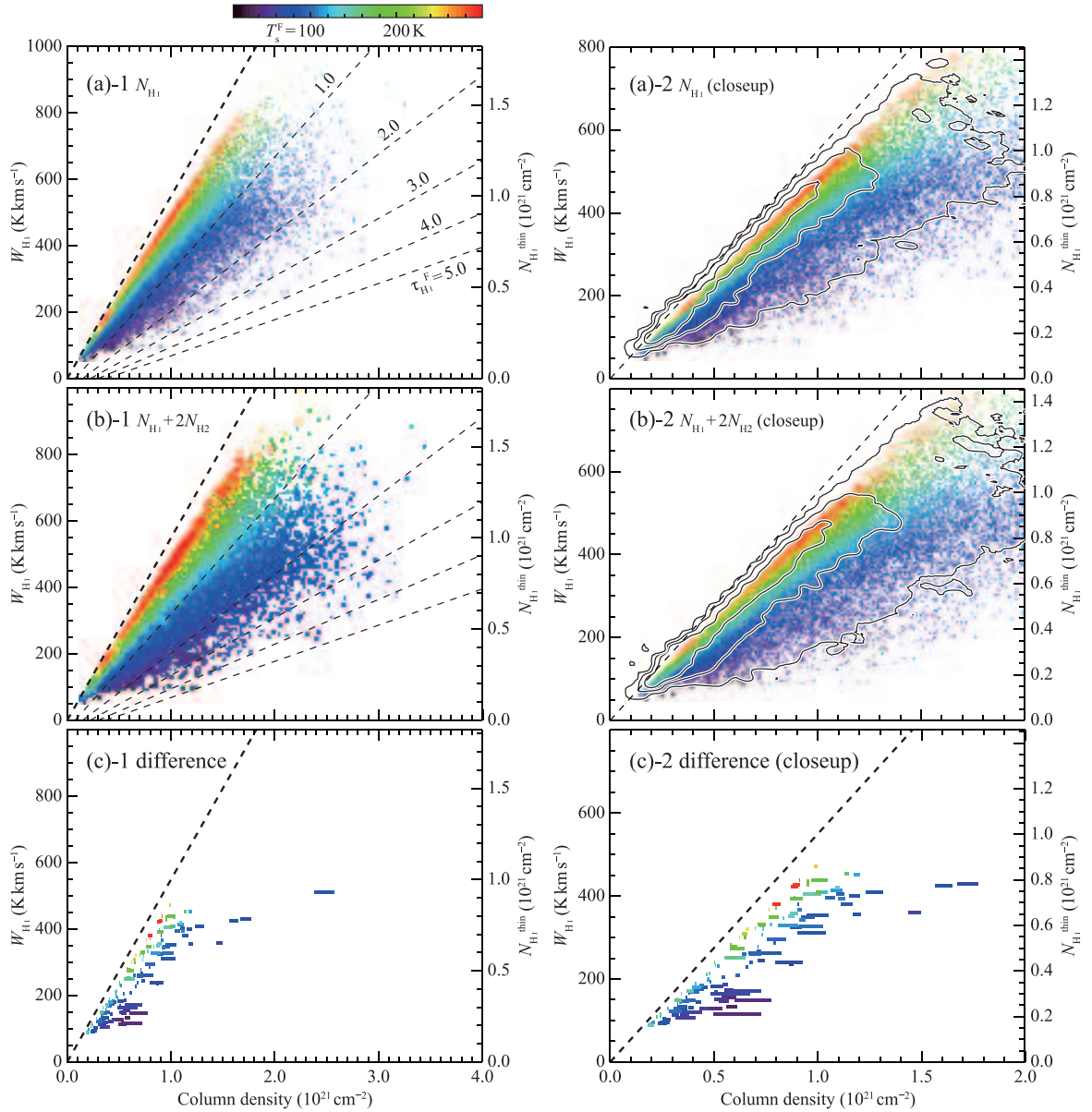


Figure 8. *Left panels:* Correlation plots of (a)-1 W_{HI} versus atomic hydrogen column density (N_{HI}), and (b)-1 W_{HI} versus total hydrogen column density ($N_{\text{HI}} + 2N_{\text{H}_2}$). Color represents T_s^F of each point. The thick dashed lines indicate optically thin limit, $N_{\text{HI}} = 1.823 \times 10^{18} (\text{cm}^{-2} \text{ K}^{-1} \text{ km}^{-1} \text{ s}) W_{\text{HI}} = N_{\text{HI}}^{\text{thin}}$, and thin dashed lines indicate W_{HI} derived with Equations (14) and (15) for $\tau_{\text{HI}}^F = 1.0, 2.0, 3.0, 4.0$ and 5.0 (from left to right in each panel). (c)-1 The difference between $N_{\text{HI}} + 2N_{\text{H}_2}$ and N_{HI} on the column density- W_{HI} plane for randomly selected 150 data points. The length of each horizontal bar shows the contribution of H_2 to $N_{\text{HI}} + 2N_{\text{H}_2}$. *Right panels:* Close-up-views of the left panels. Contours in panels (a)-2 and (b)-2 include 38%, 68%, and 95% of data points.

Table 5. Physical parameters of the three samples of H I profiles in Figure 4

	$W_{\text{H I}}$ (K km s $^{-1}$)	$N_{\text{H I}}$ (10 20 cm $^{-2}$)	$N_{\text{H I}}^{\text{thin}}$ (10 20 cm $^{-2}$)	$N_{\text{H I}}/N_{\text{H I}}^{\text{thin}}$	$\Delta V_{\text{H I}}$ (km s $^{-1}$)	T_s^{F} (K)	$\tau_{\text{H I}}^{\text{F}}$	
	(1)	(2)	(3)	(4)	(5)	(6)	(7)	(8)
Sample 1 (Figure 5(a)-1)								
whole	349	7.4	6.4	1.2	7.5	201	0.27	
CNM	103	2.6	1.9	1.4	3.0	81	0.57	
WNM	258	4.8	4.7	1.0	14.3	510	0.04	
Sample 2 (Figure 5(a)-2)								
whole	350	10.7	6.4	1.7	6.2	89	1.07	
CNM	161	6.8	2.9	2.3	3.1	64	1.87	
WNM	212	3.9	3.9	1.0	15.9	524	0.03	
Sample 3 (Figure 5(a)-3)								
whole	352	14.5	6.4	2.3	7.0	63	1.81	
CNM	212	11.1	3.9	2.9	5.0	49	2.47	
WNM	182	3.4	3.3	1.0	10.5	385	0.05	

NOTE— Columns (2): velocity-integrated intensity, (3): column density, (4): column density obtained under optically-thin assumption (Equation (1)), (5): ratio of (3) to (4), (6): line width given by $\Delta V_{\text{H I}} = W_{\text{H I}} / \max[T_b(V)]$, (7) and (8): spin temperature and optical depth given by Equations (14) and (15).

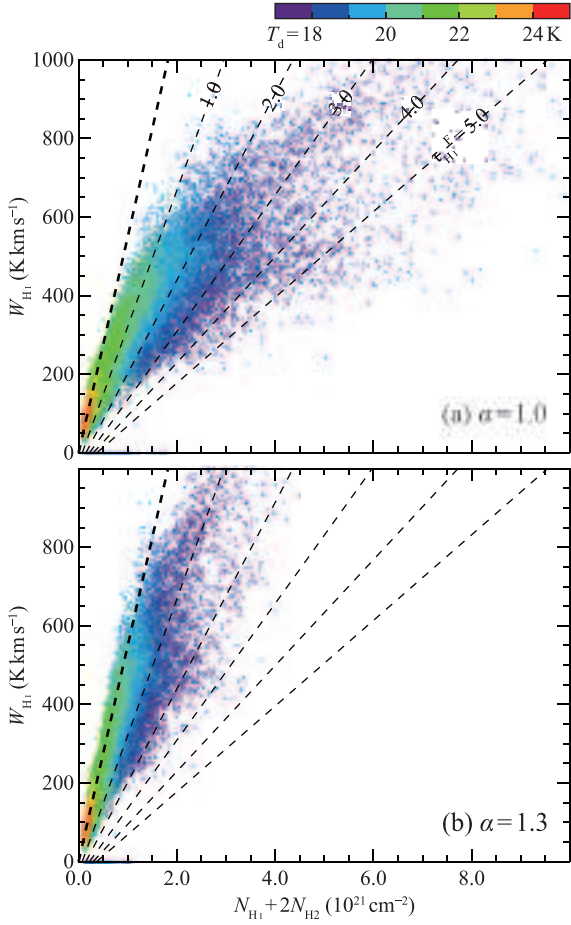


Figure 9. Scatter plots between $N_{\text{HI}} + 2N_{\text{H}_2}$ and W_{HI} for the whole sky at $|b| > 15^\circ$ compiled from the same dataset as Fukui et al. (2015). Here $N_{\text{HI}} + 2N_{\text{H}_2}$ are given from the 353 GHz dust optical depth (τ_{353} , Planck Collaboration 2014) by using $[(N_{\text{HI}} + 2N_{\text{H}_2})/N_0]^\alpha = (\tau_{353}/\tau_0)$; (a) in case of $\alpha = 1.0$, $N_0 = 1 \times 10^{21} \text{ cm}^{-2}$ and $\tau_0 = 4.77 \times 10^{-6}$ (Fukui et al. 2015), (b) in case of $\alpha = 1.3$, $N_0 = 2 \times 10^{20}$ and $\tau_0 = 1 \times 10^{-6}$ (see Section 3.5). Color represents dust temperature of each point. The thick dashed lines indicate the optically thin limits and the thin dashed lines indicate W_{HI} derived from Equations (14) and (15) for $\tau_{\text{HI}}^F = 1.0, 2.0, 3.0, 4.0$ and 5.0 (from left to right in each panel). Here ΔV_{HI} in Equations (14) and (15) is uniformly assumed to be 15 km s^{-1} .

is significantly small in the projected gas distribution. We discuss the behavior of τ_{HI} in the following.

4.1. The compact distribution of CNM

Figures 4(a) and (b) show directly the small volume filling factor of CNM which appears as sharp several density spikes with temperature lower than 300 K. Figure 4(a) shows that all these CNM spikes have peak density of $\sim 10^3 \text{ cm}^{-3}$ as compared with the background WNM density of $\sim 20 \text{ cm}^{-3}$. The typical spike size is 0.1–0.2 pc and the column density of a spike is $3\text{--}6 \times 10^{19} \text{ cm}^{-2}$. Peak τ_{HI} of one of the CNM spikes is ~ 0.3 as calculated by equation (5) for $T_s = 100 \text{ K}$ and its volume filling factor is estimated to be $\sim 5\%$ in the line of sight in Figure 4. This line of sight is typical as CNM whose total τ_{HI} is ~ 1 for 5 km s^{-1} linewidth. WNM whose temperature is higher than 300 K with density around 20 cm^{-3} has $N_{\text{HI}} \sim 10^{21} \text{ cm}^{-2}$ for a 10-pc length. WNM fills most of the volume outside of CNM.

4.2. The covering factor of CNM filaments

In projection on the sky Figures 11(a) and (b) show that τ_{HI}^F distribution is highly filamentary. We define a high τ_{HI}^F filament at $\tau_{\text{HI}}^F = 0.5$, which generally agrees with the distribution of CNM (Figure 10(a)). The filaments have a typical width of 0.1–0.2 pc (3–6 grids of the present simulations) which corresponds to the spike size in Figure 4. The projected area covering factor is shown as a histogram every $\Delta \tau_{\text{HI}}^F = 0.1$ in Figure 11(c). This indicates that the CNM filaments ($\tau_{\text{HI}}^F \gtrsim 0.5$) have a covering factor of 30%, WNM with τ_{HI}^F less than 0.5 has a covering factor of 70%. Figure 12 shows the same in Figure 11 at $4'$ resolution. The distribution is basically similar to that in Figure 11, while the $4'$ beam smears out the CNM filaments.

4.3. $\tau_{\text{HI}}^F(0.9)\Delta V_{\text{HI}}(0.9)$ versus $\tau_{\text{HI}}^F(4')\Delta V_{\text{HI}}(4')$

The covering factor distribution in Figure 11 has a significant impact on the emission-absorption measurements toward radio continuum point sources. Figure 13 shows a scatter plot between $\tau_{\text{HI}}^F\Delta V_{\text{HI}}$ at 0.9 resolution ($\tau_{\text{HI}}^F(0.9)\Delta V_{\text{HI}}(0.9)$) and at $4'$ ($\tau_{\text{HI}}^F(4')\Delta V_{\text{HI}}(4')$).

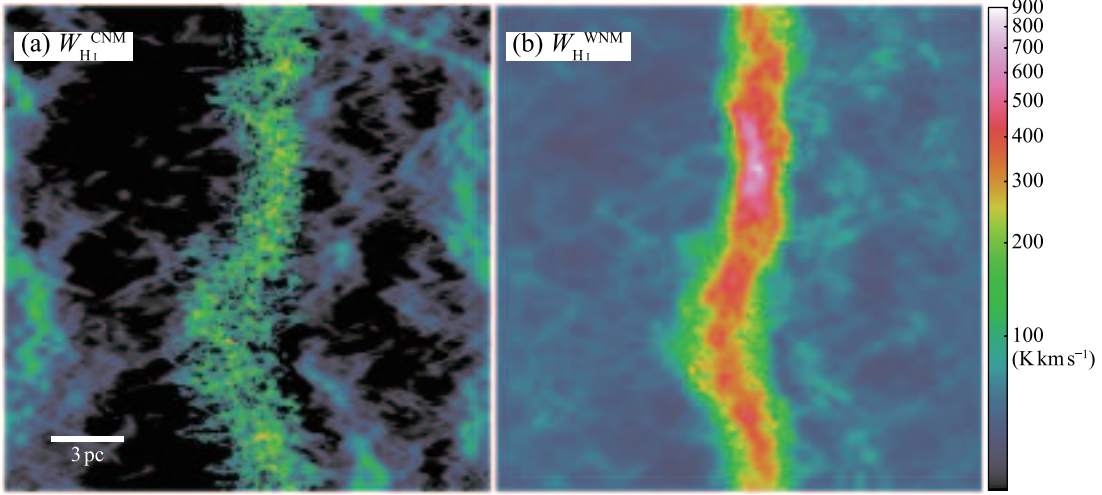


Figure 10. (a) Spatial distribution of $W_{\text{HI}}^{\text{CNM}}$ in the 0.5-Myr model which is determined by a product of $T_k < 300$ K, calculated by setting both ϵ and κ of the WNM equal to 0. (b) Same as (a) but for $W_{\text{HI}}^{\text{WNM}}$ ($T_k > 300$ K).

0'9 (spatial resolution of 0.04 pc at a distance of 150 pc) is the grid of the present simulation data (see Section 2) and 4' (0.18 pc at 150 pc) is the resolution of the Arecibo observations (Heiles & Troland 2003a,b; Stanimirović et al. 2014). We assume that $\tau_{\text{HI}}^{\text{F}}(0'9)\Delta V_{\text{HI}}(0'9)$ is substitutable for $\int \tau_{\text{HI}}^{\text{abs}}(V)dV$ by considering the resolution dependence of CNM as long as the covering factor is concerned (see Section 4.6), whereas actual $\int \tau_{\text{HI}}^{\text{abs}}(V)dV$ may fluctuate spatially more than $\tau_{\text{HI}}^{\text{F}}(0'9)\Delta V_{\text{HI}}(0'9)$. If we look at $\tau_{\text{HI}}^{\text{F}}(0'9)\Delta V_{\text{HI}}(0'9) = 1.0$, $\tau_{\text{HI}}^{\text{F}}(4')\Delta V_{\text{HI}}(4')$ is peaked at ~ 2.5 , significantly larger than $\tau_{\text{HI}}^{\text{F}}(0'9)\Delta V_{\text{HI}}(0'9)$. If we focus at $\tau_{\text{HI}}^{\text{F}}(0'9)\Delta V_{\text{HI}}(0'9) = 10$, $\tau_{\text{HI}}^{\text{F}}(4')\Delta V_{\text{HI}}(4')$ is peaked at ~ 7 , significantly smaller than $\tau_{\text{HI}}^{\text{F}}(0'9)\Delta V_{\text{HI}}(0'9)$. This variation causes a tilt of the scatter plot in the sense that the slope becomes shallower than 1.0 in Figure 13 and a regression line is given as $\log [\tau_{\text{HI}}^{\text{F}}(4')\Delta V_{\text{HI}}(4')] = 0.47 \log [\tau_{\text{HI}}^{\text{F}}(0'9)\Delta V_{\text{HI}}(0'9)] + 0.38$. These are natural outcomes of smearing out by the 4' beam. As shown in Figure 12, we do not resolve the CNM filaments at 4'. Smearing out at 4' decreases τ_{HI} toward CNM filaments, and increases τ_{HI} between CNM filaments, explaining the behavior in Figure 13(a).

4.4. Synthetic emission-absorption measurements

The results of the emission-absorption measurements toward radio continuum point sources and the emission measurements with a 4' beam are both correct, whereas τ_{HI} varies significantly due to huge difference in the volume sampled in the two measurements. Figure 14 shows results of synthetic observations of 50 radio continuum point sources which are randomly distributed toward the H I gas. The velocity integrated $\tau_{\text{HI}}^{\text{abs}}$ measured in emission-absorption substituted by 0'9 resolution are compared with velocity integrated $\tau_{\text{HI}}^{\text{F}}$ by emission measurements at 4' for the two resolutions 0'9 and 4'. The distribution is similar to what is shown in Figure 13 in that the plot shows a shallower slope than 1.0. In Figure 13 we recognize a trend that 73% of the points are seen above the dashed line with a 1.0 slope, and the trend is consistent with the large covering factor of WNM. The emission-absorption measurements are superior to the emission measurements at 4' in resolving sub-pc features including the CNM filaments. The emission-absorption measurements are however biased toward WNM with low τ_{HI} because of the large covering factor of

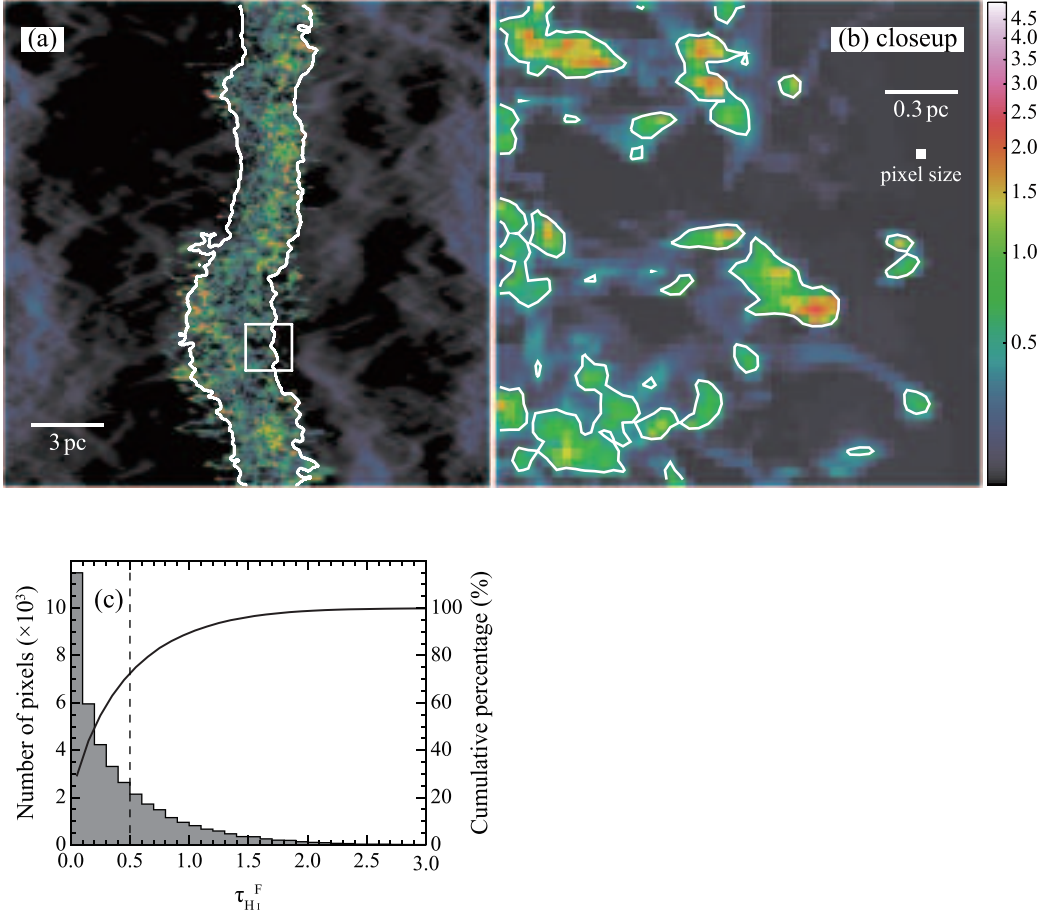


Figure 11. (a) Spatial distribution of $\tau_{\text{HI}}^{\text{F}}$ at resolution of $0.9'$ (identical to Figure 6(d)). The contour outlines the masked region applied in the panel (c). (b) Closeup-view of the bounding box shown in the panel (a). The contour is at $\tau_{\text{HI}}^{\text{F}} = 0.5$. (c) Histogram of $\tau_{\text{HI}}^{\text{F}}$. The dashed line shows $\tau_{\text{HI}}^{\text{F}} = 0.5$ and the solid curve shows cumulative percentage plotted against right-side vertical-axis.

WNM, and it is probable that the emission-absorption measurements underestimate N_{HI} due to undersampling caused by an extremely small area covering factor of the radio continuum point sources. On the other hand, the emission measurements with a $4'$ beam are accurate in measuring the total W_{HI} , whereas they are too coarse to resolve the CNM filaments. So, the two methods are not equivalent and the difference between them is a reasonable consequence of the different distributions of CNM and WNM and different resolutions. We need to choose the method depending on scientific aims.

4.5. The resolution issue

The original resolution of our simulations is 0.02 pc and the synthetic observations were made after smoothing by a factor of two into 0.04 pc , which was preferred in the present work in order to save the 3-d data size. The typical width of the CNM filaments is $\sim 0.1 \text{ pc}$, which is marginally resolved by the present grid 0.04 pc . This limited resolution is however not a problem in the above discussion on the covering factor, because the covering factor will not vary significantly as reasoned below; the mass spectrum of CNM is expressed as $dN/dM \propto M^{-1.7}$ according to the simulations as shown by Inoue & Inutsuka (2012) and Hennebelle et al. (2008). If we assume that CNM follows this relation down to lower M ,

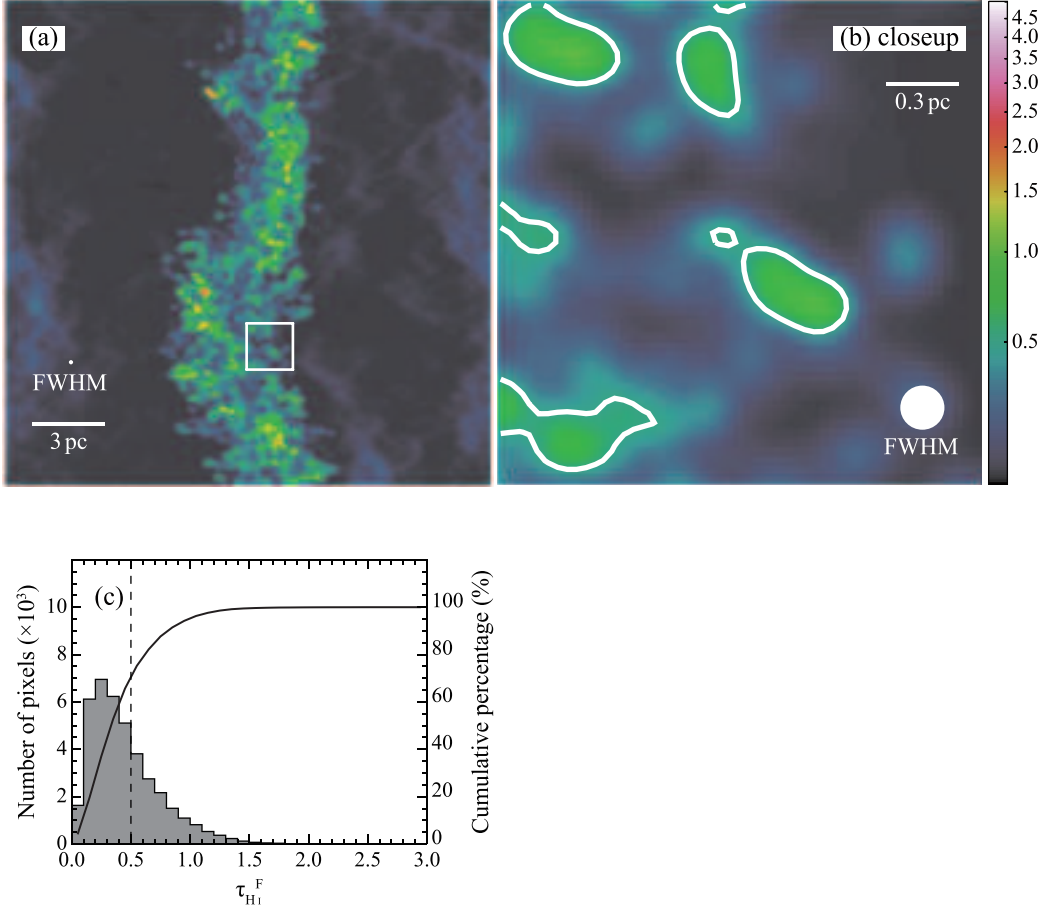


Figure 12. Same as Figure 11 but at resolution of $4'$. The $4'$ data are given from spatially smoothed N_{H_1} distribution and synthetic-observed H I spectra assuming a distance of 150 pc.

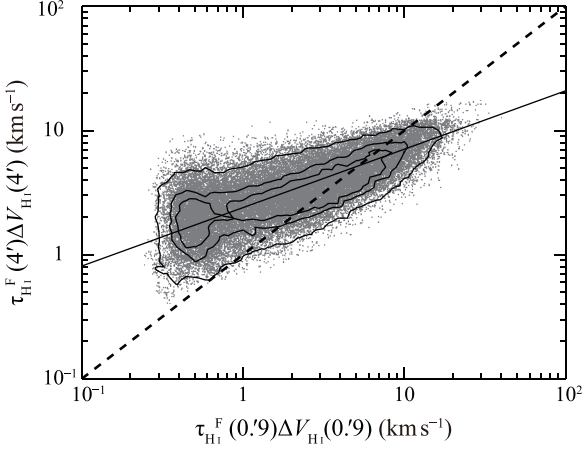


Figure 13. Correlation plots of $\tau_{\text{H}_1}^{\text{F}} (0.9) \Delta V_{\text{H}_1} (0.9)$ with $\tau_{\text{H}_1}^{\text{F}} (4') \Delta V_{\text{H}_1} (4')$. Contours include 45%, 70% and 95% of data points. The thick dashed line shows $\tau_{\text{H}_1}^{\text{F}} (0.9) \Delta V_{\text{H}_1} (0.9) = \tau_{\text{H}_1}^{\text{F}} (4') \Delta V_{\text{H}_1} (4')$ and the thin straight line shows a regression line $\log [\tau_{\text{H}_1}^{\text{F}} (4') \Delta V_{\text{H}_1} (4')] = 0.47 \log [\tau_{\text{H}_1}^{\text{F}} (0.9) \Delta V_{\text{H}_1} (0.9)] + 0.38$.

the cross section of a CNM clump S is proportional to $M^{2/3}$ if a spherical shape is assumed. The covering factor of CNM is then given by $NS \sim M^{-0.7+2/3} \sim \text{constant}$. This means spatial resolution better than sub-pc does not change significantly the covering factor and ensures our assumption to substitute $\tau_{\text{H}_1}^{\text{abs}}$ by $\tau_{\text{H}_1}^{\text{F}} (0.9)$ is appropriate (Section 4.3). In this connection, we note on the resolution in Kim et al. (2014) used in the two 21-SPONGE papers (Murray et al. 2015, 2016) was 2 pc for a total length of the simulation box 2 kpc. This grid size was chosen by the authors because these simulations were intended to be applied to a kpc scale H I distribution. A 2-pc resolution is however too coarse to resolve the sub-pc filaments of CNM (see Figures 11(b) and 12(b)) and will not be able to probe details of the

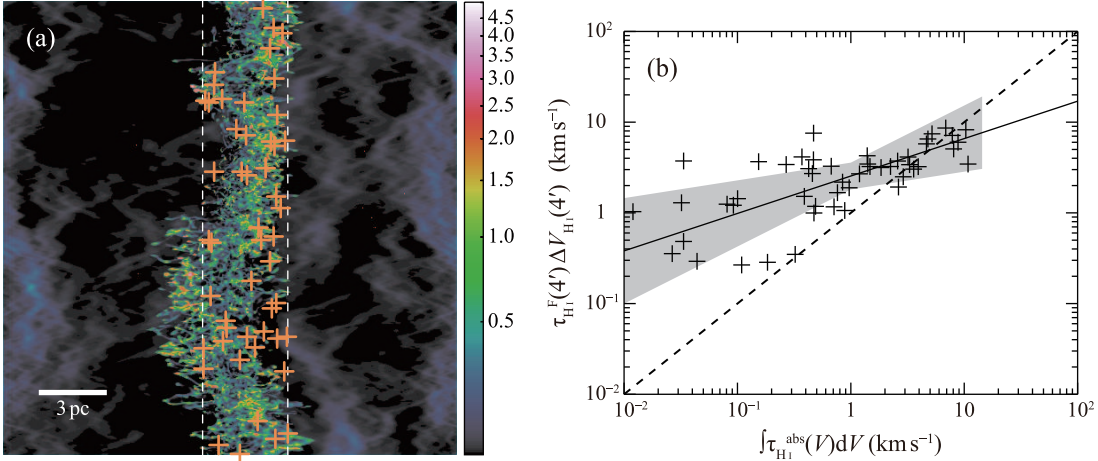


Figure 14. (a) Distribution of model radio continuum sources which are randomly distributed in the region between the two vertical lines. The background image is the distribution of $\tau_{\text{H}\,\text{I}}^{\text{F}}(0.9)$. (b) Correlation plot between $\int \tau_{\text{H}\,\text{I}}^{\text{abs}}(V)dV$ and $\tau_{\text{H}\,\text{I}}^{\text{F}}(4')\Delta V_{\text{H}\,\text{I}}(4')$ resolution toward the model radio continuum sources. The dashed line shows $\int \tau_{\text{H}\,\text{I}}^{\text{abs}}(V)dV = \tau_{\text{H}\,\text{I}}^{\text{F}}\Delta V_{\text{H}\,\text{I}}$. The solid line and shaded gray show a regression line $\log [\tau_{\text{H}\,\text{I}}^{\text{F}}\Delta V_{\text{H}\,\text{I}}] = (0.41 \pm 0.22) [\int \tau_{\text{H}\,\text{I}}^{\text{abs}}(V)dV] + (0.41 \pm 0.15)$ and its $1-\sigma$ error envelope, respectively.

emission-absorption measurements discussed in the present paper.

4.6. Comparison with Heiles & Troland (2003a,b)

Another test of the difference between the emission-absorption and emission measurements is made by a comparison with the results by Heiles & Troland (2003a,b). In Table 6 we list the relevant physical parameters toward the 79 radio continuum sources observed by Heiles & Troland (2003a,b); they are $W_{\text{H}\,\text{I}}$, $\int \tau_{\text{H}\,\text{I}}^{\text{abs}}(V)dV$ and $N_{\text{H}\,\text{I}}$ derived by emission-absorption and $\tau_{\text{H}\,\text{I}}^{\text{F}}\Delta V_{\text{H}\,\text{I}}$ and $N_{\text{H}\,\text{I}}$ derived from τ_{353} by the present work, where the nonlinear relationship $N_{\text{H}\,\text{I}} \propto \tau_{353}^{1/1.3}$ is taken into account. Figure 15 clearly shows that $\int \tau_{\text{H}\,\text{I}}(V)dV$ in emission-absorption is systematically smaller than $\tau_{\text{H}\,\text{I}}\Delta V_{\text{H}\,\text{I}}$ in emission by a factor of ~ 5 in median. Figure 16 a histogram of the ratio $N_{\text{H}\,\text{I}}^{\text{F}}/N_{\text{H}\,\text{I}}^{\text{HT}}$ shows that $N_{\text{H}\,\text{I}}$ in emission-absorption is significantly smaller than $N_{\text{H}\,\text{I}}$ in emission. The mass averaged ratio $N_{\text{H}\,\text{I}}^{\text{F}}/N_{\text{H}\,\text{I}}^{\text{HT}}$ is 1.65, lending support for an opacity correction (Fukui et al. 2015). We also find that 9 sources out of 79 have a ratio less than 1.0 (Figure 16). These positions correspond to

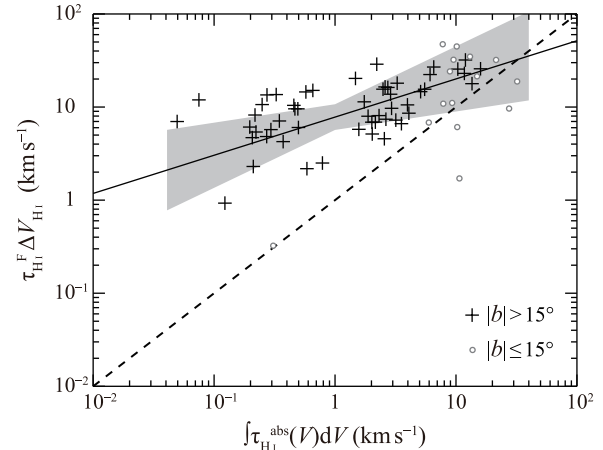


Figure 15. Correlation plot between observed $\int \tau_{\text{H}\,\text{I}}^{\text{abs}}(V)dV$ and $\tau_{\text{H}\,\text{I}}^{\text{F}}\Delta V_{\text{H}\,\text{I}}$ toward radio continuum sources listed in Table 6. Crosses and circles show $|b| > 15^\circ$ and $|b| \leq 15^\circ$ samples, respectively. The dashed line shows $\int \tau_{\text{H}\,\text{I}}^{\text{abs}}(V)dV = \tau_{\text{H}\,\text{I}}^{\text{F}}\Delta V_{\text{H}\,\text{I}}$. The solid line and shaded gray show a regression line $\log [\tau_{\text{H}\,\text{I}}^{\text{F}}\Delta V_{\text{H}\,\text{I}}] = (0.41 \pm 0.21) [\int \tau_{\text{H}\,\text{I}}^{\text{abs}}(V)dV] + (0.89 \pm 0.14)$ and its $1-\sigma$ error envelope, respectively.

the high $\tau_{\text{H}\,\text{I}}$ regions with a small filling factor in Figure 11, where $9/79 = 11\%$ is consistent with the small factor. In summary the present simulation data provide a reasonable agreement with the observed H I properties by Heiles & Troland (2003a,b).

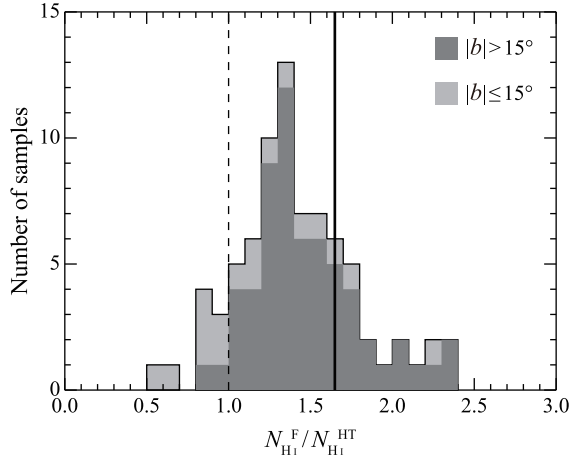


Figure 16. Histogram of $N_{\text{HI}}^{\text{F}} / N_{\text{HI}}^{\text{HT}}$. Dark- and light-gray show $|b| > 15^\circ$ and $|b| \leq 15^\circ$ samples, respectively. The vertical thick solid line shows the mass-weighted averaged ratio, 1.65, and thin dashed line shows $N_{\text{HI}}^{\text{F}} / N_{\text{HI}}^{\text{HT}} = 1$.

The numerical simulation by Inoue & Inutsuka (2012) is one of the most advanced simulations incorporating the magnetic field, density inhomogeneity and turbulence. It could be asked if the present results depend on the numerical model. Similar simulations having density inhomogeneity and turbulence were made by Hennebelle et al. (2008) by incorporating magnetic field but without H_2 formation reaction. These simulations are not suitable for the present work that requires H_2 fraction. Nonetheless, their results show similar distributions of density and temperature to those of Inoue & Inutsuka (2012) (see also Section 4.5), and their high-density cold gas shares filamentary shape with a very small area filling factor (see Figure 2 of Hennebelle et al. 2008). We conclude that the present results are consistent with these advanced numerical simulation results of H I hydrodynamics.

4.7. Recent observations of H I filaments/fibers

The spatial distribution of CNM has been a subject of H I observations since 1974. Based on aperture synthesis of the absorption toward extended continuum sources, Greisen (1973a,b)

claimed that CNM was clumpy. Subsequent observations in absorption toward extended sources and double continuum sources provided some observational constraints on the CNM distribution (Payne et al. 1982; Dickey 1979), whereas these studies were not able to constrain the covering factor of CNM. Heiles (1997) made observations toward sharp gradients in optical depth on scales of milli-arc-seconds and the results support the present conclusion about the compact structure of the CNM. Although these studies did not show that the CNM covering factor is small, the difference of the covering factor between $\tau_{\text{HI}}^{\text{F}} \lesssim 0.5$ and $\tau_{\text{HI}}^{\text{F}} \gtrsim 0.5$ is a factor of ~ 2 in the present results, which may not be large enough to be tested by the absorption studies with limited statistics.

It is interesting to note that a few recent papers indicate the existence of CNM filaments similar to those presented in the present work. McClure-Griffiths et al. (2006) pointed out such filaments, and Clark et al. (2014) made high-resolution studies to identify the H I filaments by the Rolling Hough Transformation. They named the CNM filaments “fibers” which has column density of $5 \times 10^{18} \text{ cm}^{-2}$, and N_{HI} of extended WNM is 10^{20} cm^{-2} . By unsharp masking Kalberla et al. (2016) identified CNM filaments whose N_{HI} is $10^{19.1} \text{ cm}^{-2}$ in the local ISM. These CNM filaments/fibers are well aligned with the magnetic field and have physical parameters consistent with the CNM filaments in the present simulations. Inoue & Inutsuka (2016) supported the formation of the CNM filaments and their alignment with the magnetic field based on the MHD simulations. We note the filaments/fibers appear to have a small covering factor similar to the present CNM filaments (see Figures 3 and 4 of Clark et al. 2014). To summarize, the current results on the small covering factor of CNM fall in line with these observational and theoretical works.

5. CONCLUSIONS

In the present paper we made synthetic observations of the realistic H I gas based on MHD numerical simulations. The H I gas is highly turbulent and inhomogeneous, and allowed us to directly compare the physical parameters with the observed H I profiles and to gain an insight into the interstellar H I. We summarize the main conclusions in the following;

1. The H I emission profile consists narrow and broad components. The narrow one consists of WNM and CNM, whereas the broad wing consists of only WNM whose T_s is more than 300 K. The contribution of WNM is comparable in mass to that of CNM but varies over a large range depending on the fraction of WNM. The H I absorption profile consists almost solely of CNM, where the contribution of WNM is extremely small because of the T_s^{-1} dependence of the H I opacity.
2. For a model which is constrained by the UV observations of f_{H_2} , we find that the H I emission is generally optically thick, lending support for the conclusion reached by Fukui et al. (2015). We confirmed that the W_{H_1} - N_{H_1} relation shows a systematic T_s -dependent variation. The averaged T_s derived by Fukui et al. (2015) corresponds to the harmonic mean of T_s and the H I optical depth is consistent with that calculated in the present numerical model. We also find that H_2 does not make a significant contribution in the W_{H_1} - N_{H_1} plot, and the high H I optical depth is the major cause of the apparent decrease of W_{H_1} at higher H I column density. We do not find that CO-free H_2 is important in the local interstellar space, having \sim 1-Myr crossing timescale, whereas it may be important in giant molecular clouds having \gtrsim 10-Myr timescale.

3. We explored the cause for the discrepancy between τ_{H_1} from the H I emission by Fukui et al. (2015) and the emission-absorption measurements of τ_{H_1} toward radio continuum sources by Heiles & Troland (2003a,b) and Stanimirović et al. (2014). The spatial distribution of CNM and WNM is significantly different according to the numerical simulations. CNM is highly filamentary with a small area filling factor, whereas WNM is distributed more smoothly with little small fluctuations at sub-pc scale. This causes that the majority of the compact radio continuum sources lie toward WNM with low τ_{H_1} , and offers an explanation for the small τ_{H_1} in the emission-absorption measurements. τ_{H_1} derived in emission is an averaged value over a much larger volume and leads to a significantly large value around 1 after smoothing by the large beam. These details of the CNM filaments are revealed only by a high resolution of sub-pc of hydrodynamical numerical simulations, because the CNM filaments have a width of \sim 0.1 pc. The simulations used in the 21-SPONGE used a 2-pc grid (Kim et al. 2014) which is too coarse to resolve the CNM filaments and are not appropriate to quantitatively explore the CNM distribution and absorption measurements of the local ISM.
4. The model by Fukui et al. (2015) assumes uniform gas to dust ratio based on dust optical depth measured by *Planck/IRAS* by using dust as a proxy of hydrogen column density. As shown by recent studies of A_J , dust evolution is possibly affecting τ_{353} as represented by $N_{\text{H}_1} \propto (\tau_{353})^{1/1.3}$. We see that the curvature in the observed W_{H_1} - N_{H_1} plot is consistent with such dust evolution, indicating that the modification of the N_{H_1} - τ_{353} relation is

appropriate. In conclusion, the method by Fukui et al. (2014, 2015) with modification of dust evolution gives reasonable H I density which is a factor of 1.7 larger than the optically thin approximation of H I 21 cm emission in the local interstellar space within 200 pc of the sun.

We are grateful to John Dickey for his thoughtful comments which were valuable in improving significantly the present paper. This

work was supported by JSPS KAKENHI Grant Number JP15H05694. Based on observations obtained with *Planck* (<http://www.esa.int/Planck>), an ESA science mission with instruments and contributions directly funded by ESA Member States, NASA, and Canada. Some of the results in this paper have been derived using the HEALPix (Górski et al. 2005) package. This research has made use of the VizieR catalogue access tool, CDS, Strasbourg, France.

Table 6. Physical Parameters of H I toward Radio Continuum Sources

Name	<i>l</i>	<i>b</i>	$W_{\text{H I}}$ (K km s ⁻¹)	$\int \tau_{\text{H I}}^{\text{abs}}(V) dV$ (km s ⁻¹)	$N_{\text{H I}}^{\text{HT}}$ (10 ²⁰ cm ⁻²)	τ_{353}	$\tau_{\text{H I}}^{\text{F}} \Delta V_{\text{H I}}$ (km s ⁻¹)	$N_{\text{H I}}^{\text{F}}$ (10 ²⁰ cm ⁻²)	$N_{\text{H I}}^{\text{F}}/N_{\text{H I}}^{\text{HT}}$
(1)	(2)	(3)	(4)	(5)	(6)	(7)	(8)	(9)	(10)
3C18	118°.62	-52°.72	283	3.26	5.99	1.13×10^{-5}	18.04	12.95	2.16
3C33-1	129°.43	-49°.34	154	0.37	2.81	2.10×10^{-6}	4.25	3.54	1.26
3C33	129°.44	-49°.32	154	0.27	2.78	2.16×10^{-6}	4.82	3.62	1.30
3C33-2	129°.46	-49°.27	164	0.59	2.92	1.97×10^{-6}	2.18	3.37	1.16
3C64	157°.76	-48°.20	333	2.02	6.33	6.55×10^{-6}	6.88	8.49	1.34
3C75-1	170°.21	-44°.91	412	2.49	7.97	1.11×10^{-5}	15.56	12.70	1.59
3C75	170°.25	-44°.91	409	2.73	7.89	1.09×10^{-5}	16.24	12.53	1.59
3C75-2	170°.29	-44°.91	427	2.59	8.23	1.16×10^{-5}	16.45	13.15	1.60
3C78	174°.85	-44°.51	497	3.97	10.06	1.25×10^{-5}	10.55	13.92	1.38
3C79	164°.14	-34°.45	473	3.54	9.37	9.23×10^{-6}	6.63	11.06	1.18
CTA21	166°.63	-33°.59	483	2.63	9.56	1.04×10^{-5}	7.40	12.11	1.27
P0320+05	176°.98	-40°.84	548	5.51	11.20	1.49×10^{-5}	15.54	16.00	1.43
NRAO140	159°.00	-18°.76	603	15.96	29.49	3.44×10^{-5}	25.77	30.38	1.03
3C93.1	160°.03	-15°.91	528	6.10	12.32	2.24×10^{-5}	22.35	21.87	1.78
P0347+05	182°.27	-35°.73	625	5.10	13.45	2.08×10^{-5}	14.64	20.64	1.53
3C98-1	179°.85	-31°.08	537	3.18	10.37	1.23×10^{-5}	7.24	13.80	1.33
3C98	179°.83	-31°.04	546	4.08	11.02	1.37×10^{-5}	8.59	14.99	1.36
3C98-2	179°.82	-31°.02	523	2.93	10.25	1.38×10^{-5}	9.70	15.06	1.47

Table 6 continued

Table 6 (*continued*)

Name	<i>l</i>	<i>b</i>	$W_{\text{H I}}$	$\int \tau_{\text{H I}}^{\text{abs}}(V) dV$	$N_{\text{H I}}^{\text{HT}}$	τ_{353}	$\tau_{\text{H I}}^{\text{F}} \Delta V_{\text{H I}}$	$N_{\text{H I}}^{\text{F}}$	$N_{\text{H I}}^{\text{F}}/N_{\text{H I}}^{\text{HT}}$
			(K km s ⁻¹)	(km s ⁻¹)	(10 ²⁰ cm ⁻²)		(km s ⁻¹)	(10 ²⁰ cm ⁻²)	
(1)	(2)	(3)	(4)	(5)	(6)	(7)	(8)	(9)	(10)
3C105	187°63	-33°60	526	11.97	14.68	3.38×10^{-5}	32.03	30.02	2.04
3C109	181°82	-27°77	767	11.73	20.82	3.76×10^{-5}	23.00	32.53	1.56
P0428+20	176°80	-18°55	970	13.57	23.89	3.59×10^{-5}	17.83	31.44	1.32
3C120	190°37	-27°39	517	10.35	15.94	2.93×10^{-5}	25.58	26.85	1.68
3C123	170°58	-11°66	866	10.14	27.38	6.29×10^{-5}	44.78	48.39	1.77
3C131	171°43	-7°79	1225	13.06	28.55	5.62×10^{-5}	34.83	44.34	1.55
3C132	178°85	-12°52	1098	7.85	23.81	3.08×10^{-5}	10.87	27.91	1.17
3C133	177°72	-9°91	1294	9.54	28.50	6.27×10^{-5}	32.25	48.26	1.69
3C138	187°40	-11°34	959	5.96	19.84	2.16×10^{-5}	6.82	21.28	1.07
3C141.0	174°53	-1°31	2246	10.68	52.69	5.29×10^{-5}	1.71	42.32	0.80
T0526+24	181°35	-5°19	1705	21.45	96.85	7.45×10^{-5}	32.08	55.10	0.57
3C142.1	197°61	-14°51	946	10.24	21.96	2.15×10^{-5}	6.09	21.20	0.97
P0531+19	186°76	-7°10	1221	3.68	23.84	2.08×10^{-5}	-2.63	20.61	0.86
T0556+19	190°08	-2°16	2545	32.04	53.63	1.02×10^{-4}	18.84	70.42	1.31
4C22.12	188°05	0°04	2238	27.49	85.23	6.77×10^{-5}	9.64	51.21	0.60
3C154	185°59	4°00	1748	9.30	35.58	5.29×10^{-5}	11.07	42.32	1.19
T0629+10	201°53	0°50	2470	21.29	59.25	3.98×10^{-4}	150.87	199.80	3.37
3C167	207°31	1°15	2358	15.09	50.24	5.19×10^{-5}	-1.69	41.70	0.83
3C172.0	191°20	13°41	412	0.31	7.71	5.66×10^{-6}	0.32	7.58	0.98
DW0742+1	209°79	16°59	134	-0.26	2.43	1.60×10^{-6}	3.60	2.87	1.18
3C190.0	207°62	21°84	160	-0.06	2.82	2.41×10^{-6}	8.43	3.93	1.39

Table 6 continued

Table 6 (*continued*)

Name	<i>l</i>	<i>b</i>	$W_{\text{H I}}$	$\int \tau_{\text{H I}}^{\text{abs}}(V) dV$	$N_{\text{H I}}^{\text{HT}}$	τ_{353}	$\tau_{\text{H I}}^{\text{F}} \Delta V_{\text{H I}}$	$N_{\text{H I}}^{\text{F}}$	$N_{\text{H I}}^{\text{F}}/N_{\text{H I}}^{\text{HT}}$
			(K km s $^{-1}$)	(km s $^{-1}$)	(10 20 cm $^{-2}$)		(km s $^{-1}$)	(10 20 cm $^{-2}$)	
(1)	(2)	(3)	(4)	(5)	(6)	(7)	(8)	(9)	(10)
3C192	197 $^{\circ}$ 91	26 $^{\circ}$ 40	216	0.50	3.97	3.38×10^{-6}	6.03	5.10	1.29
P0820+22	201 $^{\circ}$ 36	29 $^{\circ}$ 67	231	0.47	4.23	3.73×10^{-6}	9.57	5.50	1.30
3C207	212 $^{\circ}$ 96	30 $^{\circ}$ 13	271	2.21	5.25	1.05×10^{-5}	28.87	12.20	2.32
3C208.0	213 $^{\circ}$ 66	33 $^{\circ}$ 16	165	0.27	2.99	3.38×10^{-6}	13.50	5.11	1.71
3C208.1	213 $^{\circ}$ 60	33 $^{\circ}$ 58	151	0.33	2.76	3.12×10^{-6}	13.62	4.80	1.74
3C223	188 $^{\circ}$ 40	48 $^{\circ}$ 65	57	0.27	0.96	4.01×10^{-7}	-0.72	0.99	1.03
3C225a	219 $^{\circ}$ 86	44 $^{\circ}$ 02	183	0.57	3.40	3.53×10^{-6}	14.54	5.28	1.55
3C225b	220 $^{\circ}$ 01	44 $^{\circ}$ 00	179	1.48	3.28	4.92×10^{-6}	20.31	6.81	2.08
3C228.0	220 $^{\circ}$ 83	46 $^{\circ}$ 63	147	0.35	2.61	2.35×10^{-6}	7.09	3.86	1.48
3C234	200 $^{\circ}$ 20	52 $^{\circ}$ 70	87	0.12	1.61	7.85×10^{-7}	0.93	1.66	1.03
3C236	190 $^{\circ}$ 06	53 $^{\circ}$ 98	64	-0.14	1.21	6.95×10^{-7}	4.82	1.51	1.25
3C237	232 $^{\circ}$ 11	46 $^{\circ}$ 62	109	0.66	2.20	2.21×10^{-6}	15.10	3.68	1.67
3C245	233 $^{\circ}$ 12	56 $^{\circ}$ 30	116	0.07	2.03	2.22×10^{-6}	11.94	3.70	1.82
P1055+20	222 $^{\circ}$ 51	63 $^{\circ}$ 13	85	0.29	1.57	1.10×10^{-6}	5.72	2.16	1.37
P1117+14	240 $^{\circ}$ 43	65 $^{\circ}$ 78	86	0.22	1.57	1.50×10^{-6}	8.21	2.73	1.74
3C263.1	228 $^{\circ}$ 27	74 $^{\circ}$ 37	91	0.21	1.68	9.78×10^{-7}	2.30	1.97	1.17
3C264.0	236 $^{\circ}$ 99	73 $^{\circ}$ 64	95	0.25	1.73	1.64×10^{-6}	10.63	2.92	1.69
3C267.0	256 $^{\circ}$ 34	70 $^{\circ}$ 11	127	0.22	2.33	1.59×10^{-6}	5.39	2.85	1.23
3C272.1	280 $^{\circ}$ 63	74 $^{\circ}$ 68	132	0.20	2.39	1.73×10^{-6}	6.10	3.04	1.27
3C273	289 $^{\circ}$ 94	64 $^{\circ}$ 35	107	0.21	1.93	1.30×10^{-6}	4.69	2.45	1.27
3C274.1	269 $^{\circ}$ 87	83 $^{\circ}$ 16	124	0.46	2.36	2.34×10^{-6}	10.43	3.85	1.63

Table 6 *continued*

Table 6 (*continued*)

Name	<i>l</i>	<i>b</i>	$W_{\text{H I}}$	$\int \tau_{\text{H I}}^{\text{abs}}(V) dV$	$N_{\text{H I}}^{\text{HT}}$	τ_{353}	$\tau_{\text{H I}}^{\text{F}} \Delta V_{\text{H I}}$	$N_{\text{H I}}^{\text{F}}$	$N_{\text{H I}}^{\text{F}}/N_{\text{H I}}^{\text{HT}}$
			(K km s $^{-1}$)	(km s $^{-1}$)	(10 20 cm $^{-2}$)		(km s $^{-1}$)	(10 20 cm $^{-2}$)	
(1)	(2)	(3)	(4)	(5)	(6)	(7)	(8)	(9)	(10)
4C07.32	322 $^{\circ}$ 22	68 $^{\circ}$ 83	113	0.49	2.11	2.32×10^{-6}	9.57	3.83	1.81
4C32.44	67 $^{\circ}$ 23	81 $^{\circ}$ 04	61	0.05	1.05	8.06×10^{-7}	6.99	1.69	1.61
3C286	56 $^{\circ}$ 52	80 $^{\circ}$ 67	110	-1.26	2.04	8.14×10^{-7}	-3.84	1.71	0.84
3C293	54 $^{\circ}$ 60	76 $^{\circ}$ 06	70	-0.01	1.28	1.31×10^{-6}	15.49	2.46	1.93
4C19.44	8 $^{\circ}$ 99	73 $^{\circ}$ 04	144	-0.39	2.65	4.18×10^{-6}	15.77	6.01	2.27
4C20.33	20 $^{\circ}$ 18	66 $^{\circ}$ 83	146	0.51	2.69	1.34×10^{-6}	-1.07	2.51	0.93
3C310	38 $^{\circ}$ 50	60 $^{\circ}$ 20	190	1.57	3.71	3.48×10^{-6}	5.77	5.22	1.41
3C315	39 $^{\circ}$ 36	58 $^{\circ}$ 30	226	2.56	4.77	3.98×10^{-6}	4.57	5.78	1.21
3C318	29 $^{\circ}$ 98	54 $^{\circ}$ 78	230	2.03	4.75	4.15×10^{-6}	5.14	5.97	1.26
3C333	37 $^{\circ}$ 30	42 $^{\circ}$ 97	247	2.31	5.09	5.70×10^{-6}	8.10	7.62	1.50
3C348	22 $^{\circ}$ 97	29 $^{\circ}$ 17	289	2.15	5.69	5.70×10^{-6}	6.89	7.63	1.34
3C353	21 $^{\circ}$ 11	19 $^{\circ}$ 87	481	6.55	10.85	2.81×10^{-5}	26.92	26.03	2.40
4C13.65	39 $^{\circ}$ 31	17 $^{\circ}$ 71	473	2.88	9.16	1.18×10^{-5}	13.74	13.35	1.46
4C13.67	43 $^{\circ}$ 49	9 $^{\circ}$ 15	754	7.77	16.72	4.59×10^{-5}	47.31	37.94	2.27
3C409	63 $^{\circ}$ 39	-6 $^{\circ}$ 12	1156	8.91	25.81	4.42×10^{-5}	24.16	36.90	1.43
3C410	69 $^{\circ}$ 20	-3 $^{\circ}$ 76	2139	14.94	48.22	8.15×10^{-5}	21.40	59.04	1.22
3C433	74 $^{\circ}$ 47	-17 $^{\circ}$ 69	426	1.88	7.89	8.92×10^{-6}	7.97	10.77	1.36
3C454.0	88 $^{\circ}$ 10	-35 $^{\circ}$ 94	289	0.79	5.38	3.96×10^{-6}	2.50	5.77	1.07
3C454.3	86 $^{\circ}$ 11	-38 $^{\circ}$ 18	349	1.74	6.53	6.86×10^{-6}	11.38	8.79	1.35

Table 6 continued

Table 6 (*continued*)

Name	l	b	$W_{\text{H I}}$ (K km s $^{-1}$)	$\int \tau_{\text{H I}}^{\text{abs}}(V) dV$ (km s $^{-1}$)	$N_{\text{H I}}^{\text{HT}}$ (10 20 cm $^{-2}$)	τ_{353}	$\tau_{\text{H I}}^{\text{F}} \Delta V_{\text{H I}}$ (km s $^{-1}$)	$N_{\text{H I}}^{\text{F}}$ (10 20 cm $^{-2}$)	$N_{\text{H I}}^{\text{F}}/N_{\text{H I}}^{\text{HT}}$
(1)	(2)	(3)	(4)	(5)	(6)	(7)	(8)	(9)	(10)

NOTE— Columns (1): name of target, (2) and (3): position in the Galactic coordinates, (4)–(6): H I parameters given from [Heiles & Troland \(2003a\)](#) dataset; velocity-integrated intensity derived from expected profile, velocity-integrated optical-depth derived from opacity profile, and column density, (7): dust optical depth at 353 GHz ([Planck Collaboration 2014](#)), (8): H I optical depth derived by applying the method presented by [Fukui et al. \(2015\)](#) (see Section 3.3) (9): H I column density obtained from τ_{353} applying Equation (18) with assuming $N_{\text{H}_2} = 0$, (10) ratio of (6) and (9).

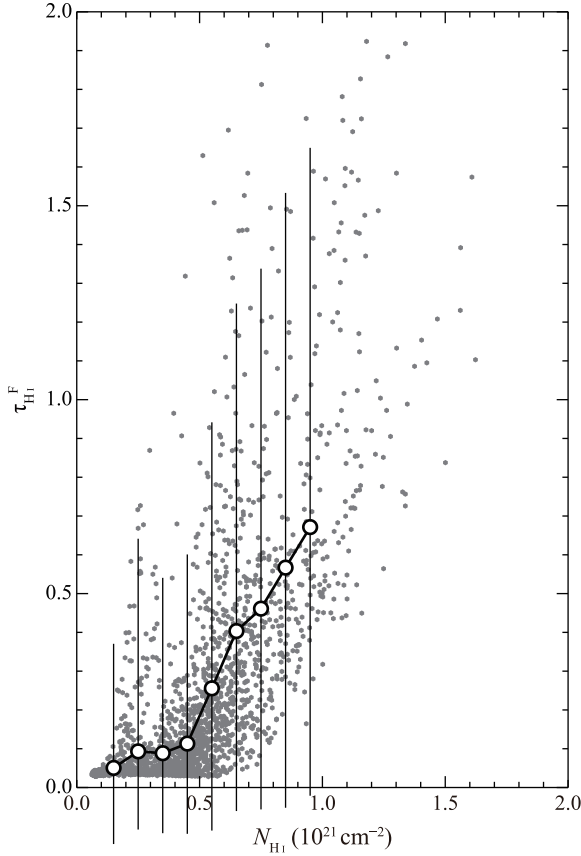


Figure 17. Scatter plot between $N_{\text{H I}}$ and $\tau_{\text{H I}}^{\text{F}}$ at $0.9'$ resolution in the bounding box shown in Figure 11(a). The circles and vertical bars show the average and standard deviation of $\tau_{\text{H I}}^{\text{F}}$ in each $1 \times 10^{20} \text{ cm}^{-2}$ bin.

APPENDIX

A. H I OPTICAL DEPTH VERSUS $N_{\text{H I}}$

Figure 17 shows a scatter plot between $N_{\text{H I}}$ and $\tau_{\text{H I}}^{\text{F}}$ at $0.9'$ resolution. These data are from a white box in Figure 11(a), which was chosen as a sample area for illustration. Figure 17 shows a fairly nonlinear growth of $\tau_{\text{H I}}^{\text{F}}$ with $N_{\text{H I}}$; for $N_{\text{H I}} = 1.5 \times 10^{20} \text{ cm}^{-2}$ $\tau_{\text{H I}}^{\text{F}}$ is as small as 0.04, whereas $\tau_{\text{H I}}^{\text{F}}$ for $1 \times 10^{21} \text{ cm}^{-2}$ reaches 0.5–2. This nonlinear behavior is explained by Equation (15); $\tau_{\text{H I}} = N_{\text{H I}} (\text{cm}^{-2}) (1.823 \times 10^{18})^{-1} [T_s (\text{K})]^{-1} [\Delta V (\text{km s}^{-1})]^{-1}$. With the increase of $N_{\text{H I}}$, both T_s and ΔV decrease mainly by less heating and more cooling. We see this trend results in strong increase of H I optical depth with $N_{\text{H I}}$, causing significantly higher contrast in Figure 6(d) ($\tau_{\text{H I}}^{\text{F}}$) than in Figure 6(a) ($N_{\text{H I}}$). Figure 4 allows us to gain an insight into the behavior of H I optical depth. In the present model the total optical depth is governed by a few dense clumps with high opacity in a line of sight (Figure 4(d)). The density $n_{\text{H I}}$ is enhanced in a clump from $\sim 10 \text{ cm}^{-3}$ to $\sim 1000 \text{ cm}^{-3}$ for a size scale of $\sim 0.1 \text{ pc}$, which is the typical Field length. $T_k = T_s$ decreases from several 1000 K to $\sim 100 \text{ K}$ in the clump, indicating a dependence of $T_s \propto n_{\text{H I}}^{-1}$. The local velocity dispersion is given by the inverse of the line shape function as $T_s^{0.5}$ (Equation (8)). Optical depth, constant $\times N_{\text{H I}} (T_s \Delta V_{\text{H I}})^{-1}$, is then proportional to $n_{\text{H I}}^{2.5} \times \text{length}$ in a line of sight, which results in a highly nonlinear dependence of H I optical depth on $N_{\text{H I}}$ as seen in Figure 17.

REFERENCES

- Banerjee, R., Vázquez-Semadeni, E., Hennebelle, P., & Klessen, R. S. 2009, MNRAS, 398, 1082
- Blitz, L., & Rosolowsky, E. 2006, ApJ, 650, 933
- Braun, R. 2012, ApJ, 749, 87
- Clark, S. E., Peek, J. E. G., & Putman, M. E. 2014, ApJ, 789, 82
- Crovisier, J., & Dickey, J. M. 1983, A&A, 122, 282
- Dickey, J. M. 1979, ApJ, 233, 558
- Dickey, J. M., McClure-Griffiths, N. M., Gaensler, B. M., & Green, A. J. 2003, ApJ, 585, 801
- Draine, B. T. 2011, Physics of the Interstellar and Intergalactic Medium (Princeton University Press)
- Ewen, H. I., & Purcell, E. M. 1951, Nature, 168, 356
- Field, G. B. 1965, ApJ, 142, 531
- Field, G. B., Goldsmith, D. W., & Habing, H. J. 1969, ApJL, 155, L149
- Fukui, Y., & Kawamura, A. 2010, ARA&A, 48, 547
- Fukui, Y., Torii, K., Onishi, T., et al. 2015, ApJ, 798, 6
- Fukui, Y., Mizuno, N., Yamaguchi, R., et al. 1999, PASJ, 51, 745
- Fukui, Y., Kawamura, A., Minamidani, T., et al. 2008, ApJS, 178, 56
- Fukui, Y., Kawamura, A., Wong, T., et al. 2009, ApJ, 705, 144
- Fukui, Y., Okamoto, R., Kaji, R., et al. 2014, ApJ, 796, 59
- Gillmon, K., Shull, J. M., Tumlinson, J., & Danforth, C. 2006, ApJ, 636, 891
- Górski, K. M., Hivon, E., Banday, A. J., et al. 2005, ApJ, 622, 759
- Greisen, E. W. 1973a, ApJ, 184, 363
- . 1973b, ApJ, 184, 379
- Grenier, I. A., Black, J. H., & Strong, A. W. 2015, ARA&A, 53, 199
- Grenier, I. A., Casandjian, J.-M., & Terrier, R. 2005, Science, 307, 1292
- Heiles, C. 1997, ApJ, 481, 193
- Heiles, C., Kulkarni, S., & Stark, A. A. 1981, ApJL, 247, L73
- Heiles, C., & Troland, T. H. 2003a, ApJS, 145, 329
- . 2003b, ApJ, 586, 1067
- Heitsch, F., Stone, J. M., & Hartmann, L. W. 2009, ApJ, 695, 248
- Hennebelle, P., Banerjee, R., Vázquez-Semadeni, E., Klessen, R. S., & Audit, E. 2008, A&A, 486, L43
- Inoue, T., & Inutsuka, S.-i. 2012, ApJ, 759, 35
- . 2016, ApJ, 833, 10
- Kalberla, P. M. W., Burton, W. B., Hartmann, D., et al. 2005, A&A, 440, 775
- Kalberla, P. M. W., Kerp, J., Haud, U., et al. 2016, ApJ, 821, 117
- Kawamura, A., Mizuno, Y., Minamidani, T., et al. 2009, ApJS, 184, 1
- Kim, C.-G., Ostriker, E. C., & Kim, W.-T. 2014, ApJ, 786, 64
- Liszt, H. 2014, ApJ, 780, 10
- McClure-Griffiths, N. M., Dickey, J. M., Gaensler, B. M., Green, A. J., & Haverkorn, M. 2006, ApJ, 652, 1339
- McKee, C. F., Parravano, A., & Hollenbach, D. J. 2015, ApJ, 814, 13
- Muller, C. A., & Oort, J. H. 1951, Nature, 168, 357
- Murray, C. E., Stanimirović, S., Kim, C.-G., et al. 2016, ArXiv e-prints, arXiv:1612.02017
- Murray, C. E., Stanimirović, S., Goss, W. M., et al. 2015, ApJ, 804, 89
- Okamoto, R., Yamamoto, H., Tachihara, K., et al. 2016, ArXiv e-prints, arXiv:1612.07696
- Payne, H. E., Terzian, Y., & Salpeter, E. E. 1982, ApJS, 48, 199
- Peek, J. E. G., Heiles, C., Douglas, K. A., et al. 2011, ApJS, 194, 20
- Planck Collaboration. 2014, A&A, 571, A11
- Rachford, B. L., Snow, T. P., Tumlinson, J., et al. 2002, ApJ, 577, 221
- Roy, A., Martin, P. G., Polychroni, D., et al. 2013, ApJ, 763, 55
- Stanimirović, S., Murray, C. E., Lee, M.-Y., Heiles, C., & Miller, J. 2014, ApJ, 793, 132
- Vázquez-Semadeni, E., Banerjee, R., Gómez, G. C., et al. 2011, MNRAS, 414, 2511
- Wolff, M. G., Hollenbach, D., & McKee, C. F. 2010, ApJ, 716, 1191